M 2025

U.PORTO
FEUP FACULDADE DE ENGENHARIA
UNIVERSIDADE DO PORTO

Topology Optimisation and Laser Powder Bed Fusion Manufacturing of a Piston and Connecting Rod

GONÇALO ALMEIDA CRUZ
MASTER'S DEGREE DISSERTATION IN MATERIAL ENGINEERING
SUBMITTED TO THE FACULTY OF ENGINEERING OF UNIVERSITY
OF PORTO

SUPERVISOR
PROFESSOR MARCO PARENTE

CO-SUPERVISOR
PROFESSOR JOSÉ COSTA

U.PORTO
FEUP FACULDADE DE ENGENHARIA
UNIVERSIDADE DO PORTO

CANDIDATO	Gonçalo Almeida Cruz	*Código*	202009561
TÍTULO	Topology Optimisation and Laser Powder Bed Fusion Manufacturing of a Piston and Connecting Rod		
DATA	9 de setembro de 2025		
LOCAL	Faculdade de Engenharia da Universidade do Porto – Sala F106 – 17:00h		

JÚRI	*Presidente*	Manuel Vieira	DEMEC/FEUP
	Arguente	Abílio Jesus	DEMEC/FEUP
	Orientador	Marco Parente	DEMEC/FEUP
	Co-orientador	José Costa	DEMEC/FEUP

“Can't Rush Greatness”

Oakley Neil Caesar-Su

ABSTRACT

This master's dissertation aims to produce a topologically optimised piston and connecting rod with higher stiffness and lower weight, subject to specified constraints, than their base models. To achieve this, Siemens NX software was used for both modelling and topological optimisation. The best iteration of the optimised piston displays a maximum displacement of 0.0800 mm while weighing only 0.45 kg, representing reductions of 35.48% and 49.10%, respectively. In the case of the optimised connecting rod, it exhibits a maximum displacement of 0.215 mm and a weight of 0.40 kg, which corresponds to a decrease of 8.51% and 31.74%, respectively. Then, to obtain smoother geometries for the optimised components, certain characteristics were remodelled.

An environmental study was carried out using Granta EduPack 2024 R2 to compare the optimised components with their base versions in terms of energy usage and CO_2-equivalent emissions. After defining all parameters for each component, including the assumption that they would be used in a sports car for ten years, it was found that the optimised piston displays a total energy usage of 2.14 x 10^6 MJ and 2.19 x 10^5 kg of CO_2-equivalent emissions, representing reductions of 32% and 21%, respectively. For the optimised connecting rod, the results were less satisfactory, with a total energy usage of 2.40 x 10^6 MJ and 1.98 x 10^5 kg of CO_2-equivalent emissions, reflecting a reduction of only 9% and an increase of 5%, respectively.

Subsequently, two optimised pistons, two optimised connecting rods, and two piston pins were produced using the Laser Powder Bed Fusion (LPBF) and Fused Filament Fabrication (FFF). For LPBF, the AISI 316L stainless steel was selected to produce the optimised piston and connecting rod separately. The Materialise software was used to define the orientation of the optimised components in the LPBF, to apply a 0.25 scale, and to set other printing parameters. For FFF, Polylactic Acid (PLA) was used and the Bambu Lab software was employed, in which the optimised piston, connecting rod, and one piston pin were scaled to 0.50, while an additional piston pin was produced at a 0.25 scale. The Bambu Lab software was also used to generate the required supports for producing the four components simultaneously.

Concluding, the topological optimisation of the piston and connecting rod was successful, producing stiffer components with significant weight reductions. This weight reduction does not only improve vehicle performance but also decreases environmental impacts, primarily by reducing the energy consumption over the component's lifetime. In terms of CO_2-equivalent emissions, it only compensates if the decrease in mass is substantial or if the component will be used for an extended period of time. Furthermore, the optimised geometries can be manufactured using LPBF technology. The components produced through FFF facilitated a more detailed comparison between the geometry obtained with the 3D model. However, further research is required, beginning with analyses of stress concentration that must be minimised, followed by fatigue performance, where simulations should be conducted, and subsequently the production of full-scale LPBF-manufactured optimised components, which should then be subjected to fatigue testing.

Keywords: Topology optimisation; Piston; Connecting rod; Environmental impacts; Energy usage; CO_2-equivalent emissions; AM; LPBF; AISI 316L; FFF; PLA.

RESUMO

Esta dissertação de mestrado visa produzir um pistão e uma biela topologicamente otimizados, apresentando uma maior rigidez e mais leve, sujeitos a certas restrições, do que os seus modelos base. Para tal, utilizou-se o software *Siemens NX* para a modelação e otimização topológica. A melhor iteração do pistão otimizado apresenta um deslocamento máximo de 0,0800 mm, pesando 0,45 kg, representando uma redução de 35,48 % e 49,10 %, respetivamente. Já a biela otimizada apresentou um deslocamento máximo de 0,215 mm e pesa 0,40 kg, que corresponde a um decréscimo de 8,51 % e 31,74 %, respetivamente. Por fim, suavizou-se as geometrias através de ligeiras alterações.

Realizou-se um estudo ambiental no *Granta EduPack 2024 R2* para comparar os componentes otimizados com as suas versões em termos de energia utilizada e emissões de CO_2-equivalente. Após definir todos os parâmetros para cada componente, incluindo que os componentes seriam utilizados num carro desportivo por dez anos, revelou-se que as partes otimizadas consomem menos energia e emitem menos CO_2-equivalente em todas as etapas do ciclo de vida, com a exceção da produção. No total, o pistão otimizado apresenta um consumo de energia total de $2{,}14 \times 10^6$ MJ e emissões de CO_2-equivalente de $2{,}19 \times 10^5$ kg, representando uma diminuição de 32 % e 21 %, respetivamente. No caso da biela otimizada, os resultados foram menos satisfatórios, apresentando um consumo energético de $2{,}40 \times 10^6$ MJ e $1{,}98 \times 10^5$ kg de emissões de CO_2-equivalente, refletindo uma redução de apenas 9 % e um aumento de 5 %, respetivamente.

Subsequentemente, produziram-se dois pistões otimizados, duas bielas otimizadas e dois pinos por *Laser Powder Bed Fusion* (LPBF) e *Fused Filament Fabrication* (FFF). Para a LPBF, selecionou-se o aço inoxidável AISI 316L e fabricou-se, separadamente, o pistão otimizado e a biela otimizada. Usou-se o software *Materialise* onde se definiu a orientação dos componentes para serem fabricados na LPBF, aplicou-se uma escala de 0,25, e estabeleceram-se outros parâmetros de impressão. Para a FFF, usou-se o software *Bambu Lab* e como material selecionou-se *Polylactic Acid* (PLA), onde se produziu com a escala de 0,50 o pistão otimizado, a biela otimizada e um pino de pistão. Adicionalmente, produziu-se outro pino de pistão, mas com uma escala de 0,25. Utilizou-se o *Bambu Lab* para gerar os suportes necessários para produzir todos os componentes simultaneamente.

Concluindo, a otimização topológica do pistão e da biela foi um sucesso, visto que se obtiveram componentes mais rígidos e leves. Esta redução de peso, além de melhorar o desempenho do veículo, também diminui o impacto ambiental, a nível da energia consumida ao longo da vida dos componentes. Em termos de emissões, apenas compensa se a diminuição da massa for elevada ou se o componente for utilizado por um longo período. Adicionalmente, as geometrias otimizadas podem ser produzidas por LPBF. Os componentes produzidos por FFF permitiram uma comparação mais detalhada entre a geometria obtida e o modelo 3D. Contudo, estudos adicionais são necessários, começando com análise de concentração de tensões que devem ser minimizadas, seguindo fadiga, onde simulações devem ser realizadas seguidas da produção dos componentes por LPBF na sua escala real, sendo estes depois sujeitos a testes de fadiga.

Palavras-chave: Otimização topológica; Pistão; Biela; Impactos ambientais; Uso energético; Emissões de CO_2-equivalente; AM; LPBF; AISI 316L; FFF; PLA.

AGRADECIMENTOS

Em primeiro lugar, gostaria de agradecer ao Professor Marco Parente por, primeiramente, ter aceitado o tema que sugeri, por toda a orientação fornecida durante a elaboração desta dissertação de mestrado, por ter respondido a todas as minhas perguntas por mais minúsculas que fossem e por me incentivado a fazer mais e melhor. Um especial agradecimento ao Professor José Costa por ter me ajudado a aprimorar ainda mais a otimização topológica e por tornar a produção dos componentes otimizados possível. Com este último tópico em mente, gostaria também de agradecer ao Ilídio Costa pelas horas gastas à volta da máquina de LPBF. Gostaria também de agradecer à Senhora Cândida, Senhora Maria José e Senhor Ramiro por toda a ajuda fornecida nos trabalhos práticos durante estes cinco anos.

Seguidamente, gostaria de agradecer à Inês Silva por todo o apoio, ajuda, encorajamento e conselhos fornecidos ao longo destes cinco anos, sem ti nada disto seria possível. Obrigado por nunca me teres deixado ir abaixo nem desistido de nada que queria.

Um sincero agradecimento aos meus pais, Camila e Rogério, por todos os sacrifícios que fizeram por mim para que eu pudesse focar na minha vida académica, nunca me irei esquecer disso. Para além disso, gostaria de agradecer por todo o apoio e carinho dados ao longo do tempo.

Adicionalmente, agradeço aos meus padrinhos, Elisabete e Pedro, por me convidarem para diversas férias ao longo dos anos e por me terem sempre apoiado.

Desejaria de agradecer ao Lourenço por, apesar dos anos passarem-se, continuar a ser sempre uma constante com quem posso contar. Gostaria também de agradecer ao Miguel e à Pena, juntamente com os restantes membros das “reuniões de condomínio”, por todas as conversas sobre temas variados, marcações e planos de viagem.

Quero também agradecer à Clara por todo o apoio e motivação fornecidos, e agradecer ao Gonçalinho por me ter dado a oportunidade de ser o seu personal coach em videojogos.

Não posso deixar de agradecer ao meu colega eterno de fundição Gonçalo por todas as conversas sobre o sistema de alimentação da peça, entre outras.

Por último, e por menos importante, gostaria de agradecer aos membros do grupo “FFAQ2”: Bruno, Filipe, Luís, Marques, Quelhas, Traila e Vitor por todas as noites haver sempre algo para aliviar a cabeça.

Gostaria de dedicar esta dissertação de mestrado ao Fernando “Nando” Tavares que, infelizmente, não pode ver o desfecho da mesma. Foste e serás sempre um avô para mim, já mais te esquecerei.

Gonçalo Cruz

INDEX

LIST OF FIGURES

LIST OF TABLES

LIST OF ABBREVIATIONS

ABS: Acrylonitrile Butadiene Styrene
AM: Additive Manufacturing
BJ: Binder Jetting
CAGR: Compound Annual Growth Rate
DCS: Datum Coordinate System
DED: Direct Energy Deposition
DFAM: Design for Additive Manufacturing
EBM: Electron Beam Melting
EDM: Electrical Discharge Machining
FDM: Fused Deposition Modelling
FEA: Finite Element Analysis
FFF: Fused Filament Fabrication
GA: Gas Atomisation
H: Hatch Spacing
ICE: Internal Combustion Engine
L: Layer Thickness
LPBF: Laser Powder Bed Fusion
MEX: Material Extrusion
P: Laser Power
PA: Plasma Atomisation
PLA: Polylactic Acid
PSD: Particle Size Distribution
RPM: Rotations Per Minute
SIMP: Solid Isotropic Material with Penalisation
SLA: Stereolithography Apparatus
SLS: Selective Laser Sintering
UV: Ultraviolet
V: Scanning Speed
VED: Volumetric Energy Density
WA: Water Atomisation

1 INTRODUCTION

1.1 Motivation

Since childhood, I have had a deep passion for the automotive world and the distinctive sound produced by combustion engines. However, in today's world, combustion engines are gradually losing prominence in the industry due to the rise of electric cars. I personally prefer vehicles powered by combustion engines over electric ones. Therefore, to contribute to the development of a more sustainable and lighter engine, I chose this master's dissertation topic: "Topology Optimisation and Laser Powder Bed Fusion Manufacturing of a Piston and Connecting Rod". Furthermore, since 2022, the Internal Combustion Engine (ICE) market has seen significant growth, with a global market size of $181.8 million, and forecasts indicate an increase in the USA at a Compound Annual Growth Rate (CAGR) of 9.3% until 2033 [1, 2]. These trends highlight that the theme of this dissertation is highly relevant both now and in the future.

The goal of this dissertation is to produce a topologically optimised piston and connecting rod with higher stiffness and reduced weight, within specified constraints. These improvements are expected to contribute to enhanced engine performance while promoting sustainability by lowering CO_2 emissions and reducing overall incorporated energy [3].

1.2 Objectives

This master's dissertation aims not only to simulate the topological optimisation of the piston and connecting rod, but also to produce both components through Additive Manufacturing (AM), using the Laser Powder Bed Fusion (LPBF) process with stainless steel 316L, as well as Fused Filament Fabrication (FFF) to manufacture larger-scale components in Polylactic Acid (PLA).

Regarding the topological optimisation, the main objective was to maximise stiffness while achieving the lightest component possible, respecting the problem constraints.

An environmental analysis was also carried out to determine whether the energy consumption and CO_2 emissions of the optimised components are smaller than those obtained through conventional methods at each stage of the components' life.

1.3 Master's Dissertation Structure

This dissertation is divided into five chapters:

- Chapter 1, the present chapter, outlines the motivation, objectives, and structure of the dissertation.
- Chapter 2 presents the literature review, beginning with an introduction to combustion engines and explanations of how each of the referred engine types operates. It then describes the components relevant to this master's dissertation, highlighting the piston and connecting rod. Further in this chapter, a section on topological optimisation is included, featuring case studies about optimised pistons and connecting rods. Additionally, a subsection on environmental analysis is included, which defines the life stages of a component, followed by a discussion of the advantages and disadvantages of AM with respect to environmental impacts. Chapter 2 finalises with a subpart

dedicated to AM, covering its evolution, general benefits and drawbacks, and focusing specifically on the processes used, LPBF and FFF, as well as the materials utilised, AISI 316L and PLA, respectively.

- Chapter 3 provides an insight into the methodology required to perform this master's dissertation. It begins by defining the software employed for modelling and optimisation. The base versions of the piston and connecting rod are then modelled. The following subsection covers the modelling of the optimised piston and connecting rod, including the definition of common construction bodies for all future iterations for both components. Another subsection presents the software used for the environmental analysis and outlines the scope of this analysis. Finally, Chapter 3 concludes with the description of the softwares used to produce the optimised components by LPBF and FFF.
- Chapter 4 presents the results and provides a discussion for the topological optimisation of the piston and connecting rod, the environmental study, their production through LPBF and FFF, and the assembly of the components.
- Chapter 5, the final chapter, summarises the key points and draws the main conclusions.

2 LITERATURE REVIEW

2.1 Combustion Engine

As stated by Basshuysen and Schäfer, “Combustion engines are machines in which chemical energy is converted to mechanical energy as a result of the combustion of an ignitable mixture of air and fuel” [4].

Combustion engines are generally classified into two categories, internal and external. However, today, only internal combustion engines are used in automobiles and motorcycles. An external combustion engine differs from an internal combustion engine by using different fluids for working and combustion [5]. Furthermore, in external combustion engines, the fuel source is burned externally [6].

In motorcycles, both 2-stroke and 4-stroke engines are available, whereas in automobiles, internal combustion engines are exclusively 4-stroke.

The 2-stroke engine is named for the two phases that occur during a single cycle, as illustrated in Figure 1.

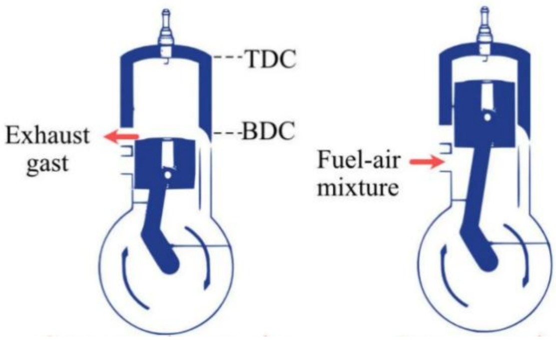

Figure 1: Cycle of a 2-stroke engine [7].

The compression stroke involves the piston’s movement from the bottom to the top position. During this motion, air or an air-fuel mixture enters the cylinder. The charge is then ignited, and combustion occurs, causing the piston to travel downwards, initiating the second phase of this engine cycle. As the piston descends, the exhaust port opens, liberating exhaust gas. From this point onwards, the cycle is restarted [7, 8].

In addition to motorcycles, 2-stroke engines can also be used, for example, in generators, chainsaws and lawn mowers. Compared with 4-stroke engines, 2-stroke engines are lighter and simpler. However, they wear faster due to the lack of a lubrication system, have higher CO_2 emissions, and consume more fuel [7 - 9].

Focusing on 4-stroke engines, these engines have four phases per cycle, as seen in Figure 2.

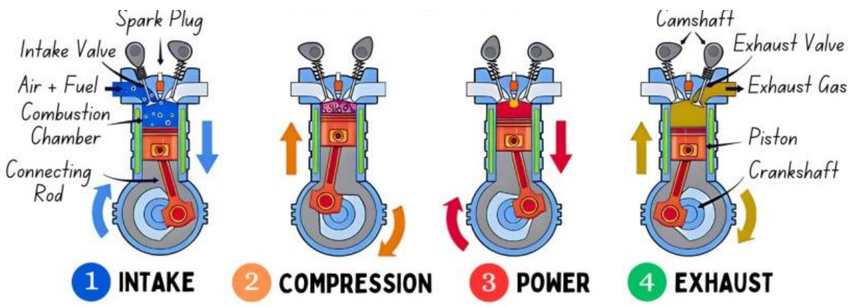

Figure 2: Cycle of a 4-stroke engine [10].

The first stage is intake, also known as the induction stroke. At this stroke, the mixture of air and fuel occurs. Afterwards, the intake valve opens, letting the mixture flow into the combustion chamber, which leads to an increase in pressure, forcing the piston to move from the top to the bottom position. The compression stroke is the second stage of the cycle, where the intake valve closes and the piston compresses the mixture, moving from its bottom position to the top. This stage is finalised once the combustion of the mixture begins, triggered by a spark. The next stage is the expansion stroke, typically known as the power stage, where, due to the combustion initiated in the previous stage, the gases rapidly expand, forcing the piston to move from the top to the bottom position, supplying the torque required to drive the connecting mechanism. To finalise the 4-stroke engine cycle, the exhaust stroke occurs. In this last stage, the piston moves from bottom to top, pushing the combusted fuel mixture out of the chamber through the exhaust valve [10, 11].

2.1.1 Piston and Connecting Rod

The piston is a moving component of combustion engines, with an upward and downward motion cycle. The main function of the piston is to convert the energy unleashed from the gas expansion to mechanical energy, making the connecting rod move, which leads to the rotation of the crankshaft [12].

The piston and connecting rod assembly consists of several components, including three piston rings, two compression rings and one oil ring, along with a piston pin, the connecting rod and the piston itself. These components, along with some others, are represented in Figure 3.

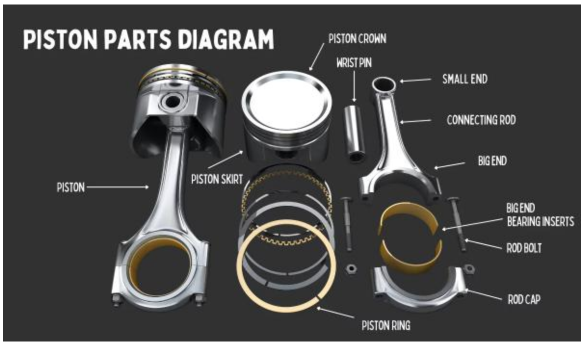

Figure 3: Components of the piston and connecting rod system [13].

The function of the compression rings is to seal the space between the piston and the cylinder, preventing combustion gases from leaking. The main task for the oil ring is to ensure the proper use of lubricant [13, 14]. The wrist pin has a simpler function, which is to guarantee that the piston and the connecting rod stay assembled. This pin works at extreme conditions with elevated temperatures, pressures and loads through many mechanical cycles [15]. The connecting rod is the mechanical component which connects the piston to the crankshaft, converting the piston’s up and down movement to the crankshaft’s rotation [13]. Finally, the piston should have the following features: piston crown, being the part in direct contact with the combustion gases, finding itself exposed to extreme temperatures and pressures; ring belt it’s where the piston rings will be added; piston skirt is the cylindrical lateral face and lastly the pin boss, which is the place where the wrist pin attaches to the piston [13, 16].

During the combustion process, the piston and connecting rod are subjected to various forces. The most relevant of which are the force originated by the pressure of gas expansion and the force applied to the connecting rod by the piston [16, 17].
There are many alternative types of engines, differing in geometrical shape, weight, power, and other characteristics. Regarding this fact, it is expected that different kinds of pistons exist. The choice of piston depends primarily on the type of engine in which it will be utilised. Figure 4 presents the main types of pistons, being flat top, dome and dish [16, 18].

Figure 4: Types of pistons [18].

Flat top pistons, which have a flat piston crown, generate high force values and enable efficient combustion. Dished pistons are commonly used in boosted applications, working at lower compression values. Dome pistons present an area which is elevated [18].
In other cases, there are pistons with an internal cooling channel, increasing the effectiveness of refrigerating the area surrounded by the combustion chamber. One final type of piston is an electron-beam-welded piston. This kind of piston involves two manufacturing processes: Forging the piston bases and welding them to cast ring bands. Producing these parts through different processes and welding them together offers numerous advantages, notably fewer defects, reduced internal stress, and a diminution of distortions [16, 19].
Focusing now on the materials of the mechanical components previously referred to, starting with the piston, which can be made of cast iron, steel or aluminium. Compared to cast irons, aluminium is lighter, whereas, with the same thickness, it has lower strength and lower wear resistance than ferrous alloys [20, 21]. Beyond the material chosen, pistons can vary in how they are produced, cast or forged. Forged pistons are typically used in motorsports due to their increased strength and durability, allowing them to operate at higher Rotations Per Minute (RPM), yet they are more expensive than cast pistons, so they are only used when required [16, 22].
Connecting rods can be produced through forging, casting, powder metallurgy or even machining. The casting process can result in connecting rods with defects that affect their durability. Although this method, like forging, is cost-effective, if a component with tight tolerances is required, approaches such as powder metallurgy or machining a forged connecting rod should be adopted [23, 24]. This component is usually made of steel. However, if a lighter connecting rod is desired, aluminium can be used, though at the expense of durability. If both lightness and strength are required, titanium is the best option when it is financially justifiable [23].
Piston pins are usually made of carburised steel, which involves adding carbon to the steel surface, followed by hardening and tempering to improve hardness. Furthermore, the pins are subjected to machining and polishing to obtain the required surface quality [25, 26].
Lastly, the piston rings are normally obtained through a process known as centrifugal

casting, which consists of pouring liquid metal into a spinning mould. Heat treatments follow centrifugal casting to improve the mechanical properties of piston rings [25, 27]. They are made of cast iron or steel because of their heat and wear resistance [25, 28].

2.2 Topology Optimisation

Topology optimisation consists of a computational design method that uses a numerical methodology to achieve an optimised solid [29]. To obtain this optimised body, it is necessary to define, firstly, the objective of the topology optimisation, which can vary from maximising stiffness to minimising mass or volume. Then, the design space, loads, and constraints are specified. The design space represents the total volume that can be optimised. The green volume shown in Figure 5 represents the design space. Some of the constraints that can be applied involve separating solids from the design space. These constraints serve, for example, to ensure that material remains in a specific volume using the Keep In function, or to guarantee that no material is present using the Keep Out function. Returning to the example in Figure 5, the brown solid was set as Keep Out, removing the section between it and the green volume. The blue solids in Figure 5 were set as Shell, meaning that the cylinder will be removed, forming a hole, while the surrounding area remains [30]. The optimised component is obtained only after all these characteristics are respected.

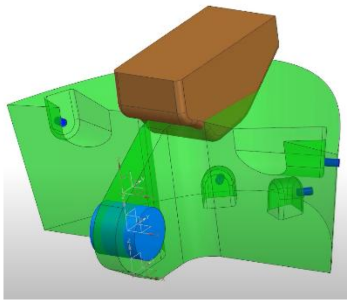

Figure 5: Illustration of the design space (green volume) and applied constraints (brown and blue solids) [30].

One of the most commonly used methods for topology optimisation is the Solid Isotropic Material with Penalisation (SIMP), which parameterises each element in the finite element mesh [31, 32]. With this, it becomes clear that the SIMP method operates based on the Finite Element Analysis (FEA), allowing the management of different objectives and constraints [33, 34].

This methodology begins with the domain discretisation, for which a finite element mesh is generated. Various sets of boundary conditions and loads are then applied to this mesh. An initial uniform density distribution is assumed for the entire mesh, with an initial value of 1. The SIMP algorithm optimises this density distribution to obtain the optimal solution while satisfying the constraints [34, 35]. During the optimisation process, each element in the finite element mesh is assigned a density (ρ), which may vary between 0 and 1 [31, 33]. The Young's modulus (E) for each element is then computed according to Equation 1, where E_0 represents the initial Young's modulus and p is the penalisation parameter.

$$E = \rho^p E_0 + (1 - \rho^p)10^{-6}E_0 \quad (1)$$

Topologically optimised components offer many advantages, such as the ability to produce lightweight alternatives to the original parts while maintaining the same, or in some cases improving their mechanical properties. Furthermore, these optimised components have a reduced environmental impact by requiring less material usage, thereby making them lighter [36].

In contrast, the main disadvantage of topological optimisation is that the resulting components often exhibit extremely complex geometries, making them impossible to produce using traditional methods. In most cases, the geometry is so complex that it can only be produced through AM.

Design for Additive Manufacturing (DFAM) enables engineers and designers to have greater freedom when creating complex geometries for a given component. Although AM allows the production of components with more intricate geometries, it still has its limitations [37]. Achieving a successful DFAM requires improvements in the technological and economic areas. In this context, the component must accomplish all the defined objectives while maintaining, and if possible, improving its properties, such as reducing its weight or even increasing its performance [36, 38]. Summarising, according to Gibson et al, the main objective of DFAM must be to "Maximise product performance through the synthesis of shapes, sizes, hierarchical structures, and material compositions, subject to the capabilities of AM technologies" [39].

2.2.1 Case Studies

More specifically, in the context of this master's dissertation, some topological optimisation of the piston and the connecting rod has already been carried out by different authors.

Starting with the piston, the following case study focuses on a steel piston for a four-stroke engine, where a half cylinder was defined as the design space. However, certain areas were excluded from the design space to preserve specific features after the optimisation. Their optimisation objective was to minimise the piston's mass. In the specific case that uses the highest force value, 40800 N, is applied to the top surface of the piston. For this scenario, two different minimum relative density values were set, 0.1 and 0.4, which resulted in the geometries shown in Figure 6 (a) and Figure 6 (b), respectively [40].

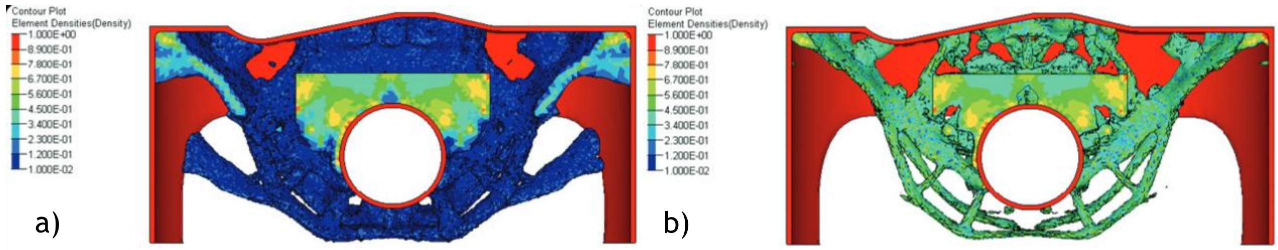

Figure 6: Optimised piston with: (a) Minimum relative density of 0.1; (b) Minimum relative density of 0.4 [40].

For the connecting rod, the objective set by the authors for the topology optimisation was to reduce weight. The same loads and constraints were applied to both the base and optimised connecting rod. The results from the optimised version display a considerable decrease in maximum stress, from 55.82 MPa to 43.86 MPa, corresponding to a reduction of 21.47%. Furthermore, the optimised connecting rod exhibits lower deformation, decreasing from 0.0488 mm to 0.0334 mm, while slightly reducing the mass from 2.144 kg to 2.121 kg. The differences between the base and optimised connecting rod in terms of geometry are notable, as shown in Figure 7 (a) and Figure 7 (b), respectively, where some material was removed from the centre of the original connecting rod [41].

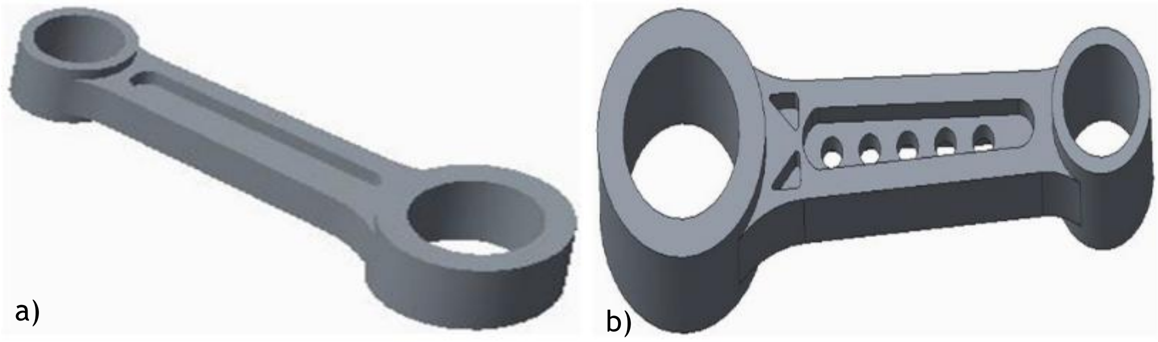

Figure 7: Connecting rod: (a) Base model; (b) Optimised model [41].

2.3 Environmental Analysis

When envisioning a futuristic industry, the image that comes to mind is that of an industry that has an extremely efficient system with minimal environmental impact. AM, as a considerable new technology with meaningful environmental benefits, contributes directly to this goal.

Before evaluating the environmental impacts of AM processes, it is necessary to understand which areas are affected. This requires comprehending the full life cycle of a component, especially of an AM component. As seen in Figure 8, the life of an AM part can essentially be divided into six stages: primary material production, feedstock production, part manufacturing, post-processing, use, and end of life [42].

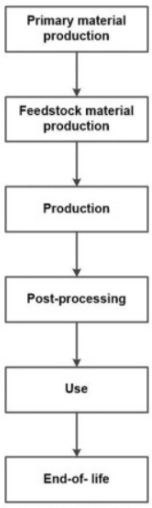

Figure 8: Life stages of an AM component [42].

Distribution is also an essential parameter that must be considered in a component's life, as it occurs between each stage and should be as efficient as possible, with minimal environmental impact. When comparing the life of a component produced through AM with one produced through conventional methods, it becomes apparent that the AM process is more complex due to the additional phases required for feedstock production and, in most cases, the necessity for post-processing. However, in many situations, the environmental advantages offset this characteristic and even other disadvantages.

To properly analyse the life of a component, as stated in ISO 14044:2006, it is necessary

to consider every input and output of each stage, including resources used, CO_2 emissions, and embodied energy [42, 43].
One of the main environmental benefits of AM is its use of minimal material to manufacture a certain component, thereby minimising material waste, particularly in LPBF, which also offers the additional advantage of reutilising the unmelted powders [44]. Although AM allows the production of near-net-shape parts, it still generates some material waste, including powder that cannot be recycled, material used for supports, and material removed during post-processing [42, 44, 45].
Utilising less material implies the production of lightweight components, which is another significant advantage, as it can drastically decrease fuel consumption and CO_2 emissions over the component's lifetime, particularly in the automotive and aerospace sectors, affecting not only the use phase but also distribution [44, 46]. Due to the diminished lead time provided by AM, it becomes unnecessary, or at least significantly less necessary, to maintain warehouses stocked with, since they can be quickly produced when required, which represents not only a great economic advantage but also an environmental one through reduced energy consumption [47, 48]. AM enables the possibility to extend the product life of a component by repairing it. [46, 49]. The last main environmental benefits of AM are the ability to produce complex geometries without the need for additional steps and the possibility of replacing multiple assembled parts with a single component, thereby reducing the energy that would be required using conventional methods [44, 50].
Concentrating now on the environmental downsides of AM, beginning with the additional stage previously mentioned in the life of an AM component, feedstock production. This requirement increases the embodied energy of an AM part, particularly in the production of metal powders for LPBF, where higher energy consumption and the use of inert gases result in significant environmental impacts [51, 52]. Beyond inert gases, sound is also a form of pollution generated by AM. Yet a more critical health hazard arises from continuous exposure to these processes without proper precautions taken into consideration, such as the inhalation of particles and volatile organic compounds, which can cause nausea, headaches, chest pain, and worse, lung diseases [51, 53]. Furthermore, when the powder cannot be reused, it must be disposed of according to the law in order to minimise its environmental impact [54]. As referenced before, metal AM usually involves additional phases in the component's life, one of which is post-processing, notably machining, used owing to the poor surface quality on AM components, improving the surface finish, increasing the total energy consumed, and the total costs in AM processes [42, 55]. In addition to AM environmental drawbacks, these types of processes present a higher rejection rate, augmenting the percentage of lost material and thereby escalating the general environmental impacts [51, 56].

2.4 Additive Manufacturing

Additive Manufacturing (AM) is a layer-by-layer process based on specific CAD data [57]. In other words, as presented in ISO/ASTM 52900, AM is a "process of joining materials to make parts from 3D model data, usually layer upon layer, as opposed to subtractive manufacturing and formative manufacturing methodologies" [58].
The history of AM begins in 1981 with Dr. Hideo Kodama, who developed the first additive

manufacturing machine that worked by exposing photopolymer material to light to produce prototypes. Dr. Kodama used his machine to create a model house, and the result can be seen in Figure 9 [59, 60].

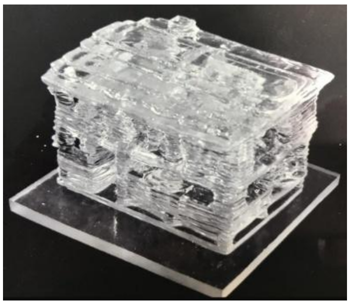

Figure 9: Model house produced by Dr. Kodama [61].

In the mid-to-late 1980s, Chuck Hull patented the first AM technology, Stereolithography Apparatus (SLA). This process consists of depositing a layer of Ultraviolet (UV) photopolymer resin and then curing it as intended with a UV laser. When this layer is finished, the platform lowers and adds a new layer, restarting the process until the model is completed [62, 63]. Before developing this technology, Chuck Hull had already set his goal: to quickly prototype plastic parts and thereby increasing the speed of the design cycle for new parts. The first model he produced with SLA was a small cup, presented in Figure 10 [64].

Figure 10: First model produced with SLA [64].

Between 1987 and 1989, LPBF was developed and patented by Carl Deckard and Joe Beaman. During this period, LPBF was known as Selective Laser Sintering (SLS), which could produce complex geometries by melting material particles with a laser beam [65, 66]. A more in-depth explanation of how this process works will be provided later in this chapter. Finally, in 1990, the first additive manufactured metal part was produced by Professor David Bourell and Manriquez-Frayer. This part was a small gear made with 70Pb-30Sn alloy, shown in Figure 11 [66].

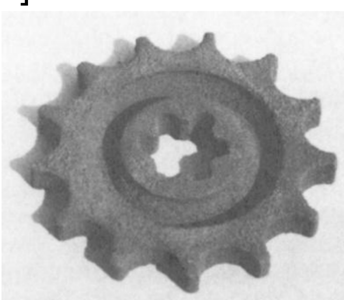

Figure 11: First additive manufactured metal part produced [66].

Scott Crump invented the first Material Extrusion (MEX) process in 1988, naming it Fused Deposition Modelling (FDM). This process consists of extruding liquefied filament feedstock and depositing it layer by layer until the desired part is finished. One year later, Scott founded Stratasys and registered a patent based on this technique [65, 67].
Over the years, the previously mentioned technologies have been improved, and new ones have been created. Nowadays, due to this evolution, AM is acknowledged not only as rapid prototyping but also as a viable alternative to conventional processes [68].
Although AM is a relatively recent technology, it presents a variety of advantages over traditional processes, such as the ability to produce extremely complex geometries without increasing costs. One example is the creation of intricate internal features, like internal channels, that would otherwise be impossible to produce [69, 70]. Another positive point, which is directly related to the previous one, is the mass customisation. This means that a certain component can be strongly customised as requested by the client at reasonable costs to the producer [38, 69]. AM can be employed to repair a damaged component, serving as a quick solution that enables continued functionality while awaiting the arrival of the replacement component. A study concluded that using AM technology followed by machining to repair a gear with one damaged tooth is a fast and effective option, presenting a good metallurgical bonding [71]. An additional advantage of AM is the potential to produce multiple components welded together at once, creating a single part with the same purpose. This is demonstrated by GE Aviation, which produced the fuel nozzle injector seen in Figure 12, replacing 20 components that were welded and brazed together [72].

Figure 12: Fuel nozzle injector produced by GE Aviation [72].

Unfortunately, AM not only has positive aspects but also has its flaws. The most common disadvantages of AM processes are the limited availability of suitable materials, with only a few available metal alloys such as, titanium, stainless and tool steel, aluminium, and resins, ceramics, composites and polymers in the form of powders and wires, which is minimal in comparison extensive variety of materials that are accessible in traditional processes [73, 74]. Lack of repeatability and the low production rate are two other main disadvantages of AM processes, especially when compared with conventional methods [73, 75]. AM components may require supports to produce the desired part, usually when the overhang angle exceeds 50º, which increases material consumption and necessitates their removal after production [75, 76]. Anisotropic structures are a serious challenge in this type of process, as the component will exhibit varying mechanical properties depending on the orientation in which the force is applied [77]. Another main drawback of AM techniques is the poor surface finish resulting from a layer-by-layer process, which forms an effect referred to as stair casing, as seen in Figure 13. To achieve the required surface finish, it is usually necessary to perform post-processing operations such as machining [75, 78].

Figure 13: Stair casing effect [78].

There are certain other disadvantages of additive manufacturing. However, one important drawback that is rarely taken into consideration is the ease with which weapons can be created [75].

2.4.1 Laser Powder Bed Fusion

Laser Powder Bed Fusion (LPBF) is, as its name indicates, a powder bed fusion AM process, similar to Electron Beam Melting (EBM). The main difference between LPBF and EBM is primarily differentiated by how each one melts the metallic particles: one uses a laser and the other uses an electron beam as the energy source, respectively [79, 80].

As with all AM methods, it is first necessary to have the desired 3D model prepared, slice it, and then define the required parameters. Focusing now specifically on the LPBF process, the chamber must be protected with an inert gas, such as argon, to prevent any oxidation or contamination during the production of the component [81, 82]. Once an inert atmosphere is established in the chamber, the feed piston rises and the recoater arm spreads the first layer of powder over the platform, then the blade ensures that only one layer is present on the bed. Afterwards, the laser melts the precise powders to produce the current layer of the component. When the first layer is finished, the platform lowers and a new layer of powder is spread over the previous one, restarting the cycle until the desired part is obtained [82]. A representative scheme can be seen in Figure 14.

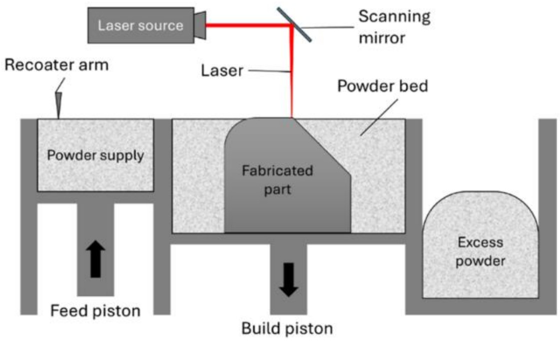

Figure 14: Scheme of the LPBF process [83].

Subsequently, the remaining powder inside the chamber must be vacuumed out, revealing the produced component. However, this component is fused to the LPBF platform, so both must be removed during a post-processing phase.

Suitable materials for LPBF mainly include steel, aluminium, and titanium alloys, yet other alloys such as nickel, copper, and zinc are also used [80, 84]. Some examples of steels used in LPBF include 2507 duplex SS, maraging, and 316L, due to their generally great mechanical properties. A more in-depth analysis of the 316L will be presented in the following subchapter of this master's dissertation. The main aluminium alloys used in LPBF are AlSi12 and AlSi10Mg, primarily valued for enabling the creation of lighter structures than those made of steel. Lastly, titanium alloys, such as Ti6Al4V, typically offer the best of both worlds by combining great mechanical properties with low weight, making them ideal for lightweight components [84].

Components produced by LPBF can be applied across a wide range of fields, namely biomedical engineering, aerospace and spacecraft, automotive, and even oil and gas extraction [81, 82]. Some examples of biomedical components produced by LPBF include customised medical implants designed to meet the specific needs of each patient, including a polylactide/calcium carbonate composite for a cranial implant, as shown in Figure 15. Furthermore, NiTi stents and dental braces, owing to their superelastic properties, are additional cases of medical devices produced by LPBF [82, 85].

Figure 15: Cranial implant [85].

In the aerospace industry, LPBF components play an essential role, and their importance has grown over the years. Components produced through this method include heat exchangers, turbine blades and discs [86, 87]. One specific example is illustrated in Figure 16, showing a high-pressure turbine blade made from Inconel 718. This turbine, produced through LPBF, offers a major advantage, which is the ability to create complex internal geometries such as internal cooling channels, enhancing efficiency and longevity while reducing its overall weight [87, 88].

Figure 16: Turbine blade manufactured using LPBF [87].

LPBF is a complex process, involving many different parameters that must be properly controlled to minimise the occurrence of defects. Before setting the parameters, it is necessary to select the desired laser. This choice essentially depends on the material to be used. The lasers commonly utilised in LPBF are infrared due to their high efficiency, and are mainly divided into two categories, CO_2 and fibre lasers [65]. When comparing fibre with CO_2 lasers, components produced with the first one exhibit superior detail and lower porosity. Although infrared lasers are highly efficient, their effectiveness does not extend to all materials. In particular, they have special difficulties producing copper or gold components due to their low absorption coefficients, which cause most of the laser energy to be reflected. In such cases, green or blue lasers can be used as alternatives. Green lasers allow improved absorption in these materials, but they are more expensive and less stable. Blue lasers also provide higher absorption in copper and gold than infrared lasers and offer smaller spot sizes, which increases resolution and accuracy. The best alternative to infrared lasers for producing parts in copper or gold is blue lasers, yet they are even more expensive than green lasers [89, 90].

The selected powder for this process must be under strict control regarding its characteristics, since two powders of the same alloy can result in significantly different mechanical properties if their characteristics are not properly controlled. Starting with powder morphology and Particle Size Distribution (PSD), spherical powders with a broader PSD are preferred, because the smaller particles can fill the interstices between the larger ones, thereby increasing the powder compactability [91]. Another crucial factor that directly affects the mechanical properties is the chemical composition of each particle. Ideally, all of them should have a similar chemical composition [81].

The quality of the final product is also affected by the parameters set in LPBF, namely Laser Power (P), Scanning Speed (V), Hatch Spacing (H), and Layer Thickness (L) [81, 82]. Among these, P has a significant influence on determining the microstructure, mechanical properties, and even the surface quality of the final component [92]. V, as its name indicates, is the speed at which the laser moves during the production of the desired component, and just like P, it directly influences the resulting microstructure and mechanical properties obtained by affecting the temperature and size of the molten pool [93]. H is defined as the distance between two bordering laser passes, being critically involved in porosity and, analogous to the previously mentioned parameters, has a direct impact on the microstructure and mechanical properties [94]. Lastly, increasing L improves productivity but may also lead to a higher percentage of defects in the final component, reducing its mechanical properties [95]. Usually, a more refined powder is preferred, as it can lead to better mechanical properties. However, if a powder with an extremely small particle size is used, it can decrease both efficiency and mechanical properties of the component due to the formation of a powder cloud. All these parameters are interrelated through the Volumetric Energy Density (VED), demonstrated in Equation 2, which is essential for controlling the resulting microstructure and the defects obtained [82, 96].

$$VED = \frac{P}{VHL} \tag{2}$$

VED is expressed in joules per cubic millimetre. If it is too high, it will cause material evaporation, leading to the keyhole effect, whereas if it is too low, there will not be enough energy to melt the powder fully [81].

Keyhole mode is one of the three modes available in LPBF, using an elevated VED value that boils the metal powder and creates a depression in the liquid metal [97, 98]. Furthermore, this effect can be classified as either stable or unstable, where reaching the unstable regime can create isolated cavities with trapped air that, once the surrounding liquid solidifies, will result in keyhole porosity [97 - 99]. The keyhole mode is illustrated in Figure 17, which also shows the imprisoned air that leads to keyhole porosity.

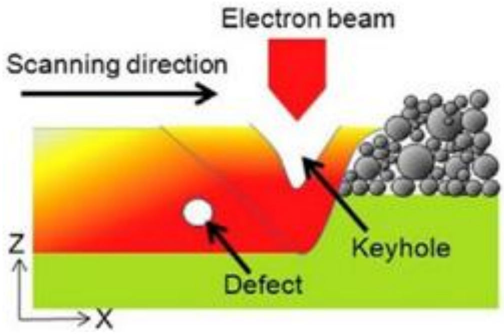

Figure 17: Trapped air during the keyhole method [81].

Sadly, the disadvantages of LPBF are not limited to keyhole porosities, as it also exhibits many general disadvantages of AM previously mentioned, including anisotropy, cracks, poor surface finish, and even a lack of materials available, especially due to the required small particle size [81, 100, 101]. Besides these more common defects, LPBF also presents specific drawbacks. For instance, components produced are limited by the build plate size, and numerous parameters must be precisely controlled to produce a component as defect-free as possible, which increases the overall complexity of the process [86, 101]. When compared to other AM processes, LPBF is one of the most expensive, both in terms of equipment and maintenance, and if the necessary precautions are not taken into consideration during operation, the metal powder can be inhaled, causing serious health problems, or the laser can result in permanent injuries [100, 102]. Furthermore, LPBF always necessitates post-processing operations in order to separate the produced component from the base.

As expected, LPBF offers many of the well-known advantages associated with the AM process, notably the capacity to produce components with highly complex and customised geometries without increased costs, as well as the ability to manufacture them in a short time without the need for a mould [87, 103]. LPBF also provides some advantages that are characteristic of itself, such as the ability to produce parts near full density, and, as already referred, it operates in an inert atmosphere, which is a major benefit as it prevents oxidation and contamination that would otherwise happen in traditional methods, predominantly with reactive metal alloys like titanium [81, 104].

2.4.1.1 AISI 316L Stainless Steel

The AISI 316L powder can be produced through essentially three processes: Water Atomisation (WA), Gas Atomisation (GA), or Plasma Atomisation (PA). Starting with WA, as seen in Figure 18, this process begins by melting the desired metal, after which a nozzle its opened to allow the molten metal to fall into the atomisation chamber, where it is sprayed by water, rapidly solidifying and forming metal powder that is gathered at the base of the camber mixed with water, which has to be removed [105].

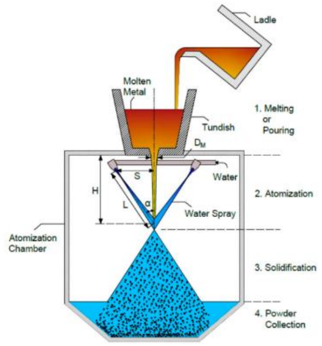

Figure 18: WA process [105].

GA is quite similar to WA, except that it uses high-pressure gas instead of water and operates in an inert atmosphere or vacuum [106]. Finally, PA, instead of directly using molten metal, utilises metal wire that is heated by plasma torches and resolidifies into metal powders, and similarly to GA, it operates in an inert atmosphere or a vacuum chamber [106, 107]. Among these three methods of powder production, PA yields powders with the smallest particle size, the highest sphericity, and the purest powders. Still, due to its low production rate and extremely high costs, PA powders are not as commonly used as those produced by WA or GA [106 - 108]. Therefore, the best compromise is GA, as it produces spherical geometries with superior mechanical properties, such as higher yield strength and elongation when compared with WA, because this process typically results in powders with irregular shapes, lower mechanical properties, larger particle size distribution and the existence of an oxide layer [108 - 110]. GA presents even more advantages over WA, including the capacity to produce denser components with lower surface roughness while maintaining dimensional accuracy, but WA still offers benefits in terms of a higher production rate and cheaper powders. [108 - 110].

AISI 316L is typically used in AM, especially in the LPBF process, as a result of its high thermal conductivity, which helps prevent elevated thermal gradient and thereby reduces internal stresses, while enabling a favourable solidification rate and maintaining a low cost [111, 112].

Mechanical properties of the AISI 316L will firstly depend on the selected manufacturing method, whether it is a conventional or an AM process. Conventional methods, such as casting or forging, can present lower tensile strength, yield strength, and hardness when compared to AM processes [113, 114]. Still, components manufactured with AISI 316L through AM processes display lower ductility and tend to develop defects, particularly, anisotropy and porosity, ultimately making the material more brittle [114]. Within the AM processes, the mechanical properties vary depending on the selected method. When focusing particularly on LPBF, the mechanical properties of the produced component depend, as previously mentioned, on the selected parameters. Furthermore, AISI 316L generally exhibits great mechanical properties, such as microhardness between 160 and 240 HV, yield strength above 300 MPa (reaching up to 550 MPa in some cases), and an ultimate tensile strength of around 600 MPa [114 - 116]. Additionally, this material provides significant benefits in terms of corrosion resistance and biocompatibility [112, 114].

All these advantages and characteristics of the AISI 316L make it suitable for various

sectors, namely the bio-medical, petrochemical and chemical industries, as well as the aerospace and automotive fields [111, 112]. AISI 316L serves many functions in the healthcare sector, such as plates, screws, orthopaedic bone fixation devices, hip prostheses, and dental implants, among many others, due to its biocompatibility, corrosion resistance, and lower cost compared to titanium [112, 117, 118]. Nowadays, beyond the medical applications mentioned, AM AISI 316L is being studied for use in stents and implants customised to meet the needs of each patient, although it still faces several challenges that must be overcome to achieve the required medical standards [119, 120]. AISI 316L is used in the petrochemical and chemical industries due to its enhanced corrosion resistance even at elevated temperatures, being particularly utilised in filtration components, while the design freedom provided by LPBF enables the production of complex geometries at a considerably low cost and with reduced environmental impact [112, 121]. Now, focusing on the aerospace field, owing to the previously mentioned characteristics of this steel, AISI 316L is eligible for aerospace components with studies showing that this material produced through LPBF can be a viable alternative to conventional methods in this sector, for example in brackets where parts manufactured via LPBF display similar or even superior mechanical properties compared to those produced by conventional methods [113, 122].
The last field is automotive, where some components made of AISI 316L are being studied for fabrication through LPBF, such as hydraulic and intake manifold, gears, and exhaust filter [123, 124].

2.4.2 Fused Filament Fabrication

Fused Filament Fabrication (FFF) can also be referred to as FDM, as both terms describe the same process. However, FDM is a trademark owned by Stratasys, whereas FFF is a generic term that involves all brands. As previously explained in this chapter for the FDM process, the FFF involves extruding liquefied filament feedstock and depositing it layer by layer to form the desired part, along with the necessary supports, that should ideally be easy to remove once manufacturing is complete [67]. Once each layer is deposited, the build platform lowers or the head rises, according to the layer thickness. A simple representation of this process is displayed in Figure 19.

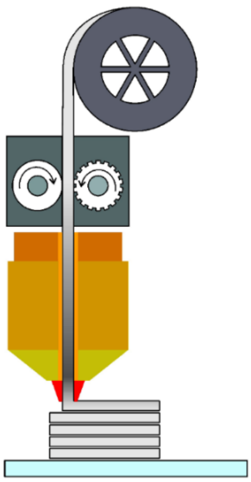

Figure 19: FFF process [125].

This process is commonly used to produce thermoplastic parts, with Acrylonitrile Butadiene Styrene (ABS) and PLA being the most widely used materials. Although typically applied to polymers, it can also be utilised to produce composites with a polymeric base reinforced with carbon fibres, wood fibres, bamboo fibres, and even metals such as steel and copper, where the reinforcement percentage can, in some cases, reach up to 40% of total volume [125].

FFF presents many advantages, with the most notable being that it is the cheapest AM process, offering a safe production environment as it does not require inert gases, powders, or lasers. Additionally, it allows simultaneous usage of different materials, which are available in a considerably wide variety and distinct colours [125]. Further advantages, common to other AM processes, include the ability to produce complex geometries without increases in price or time, allowing the creation of customisable and lightweight parts [126].

Considering all these advantages, it is to be expected that FFF products find application in various areas, such as toys, prototypes, automotive and aerospace components, as well as in the mould-making industry [126, 127].

Even though FFF presents several interesting advantages, it is not a perfect process, as it also has notable weaknesses including generally poor surface quality, anisotropy, a limited material selection compared to traditional methods, and, in some cases, higher material usage due to the need for supports that enable the component's production in the first place [125, 126].

2.4.2.1 Polylactic Acid

Polylactic Acid (PLA) is one of the most used materials in FFF because it is relatively easy to utilise. It requires a low extrusion temperature, does not need a heated base, and can produce satisfactory results with low production costs, as it consumes relatively little energy and is an inexpensive material [128].

Using PLA as the material for FFF presents even more advantages beyond those already mentioned. For example, during the production process, it does not emit toxic gases into the atmosphere, making it suitable for enclosed environments. Additionally, the produced parts are rigid, offer greater tensile strength than other thermoplastics such as ABS, and are also biodegradable [128, 129]. However, PLA has some drawbacks, as components produced with this material should not be used in environments exposed to moderately high temperatures, due to low resistance above 60 ºC. Although PLA results in rigid parts, they are brittle and have low toughness [128, 129].

One of the main applications for PLA components produced through FFF is in the decorative sector, due to the ability to create complex geometries in a variety of material colours [129]. Since PLA can be reinforced with different materials to create composites, it also finds applications in various fields, including automotive and aerospace components.

3 MATERIALS AND METHODOLOGY

3.1 Materials

The material chosen for this master's dissertation was the AISI 316L stainless steel, which is typically used in various AM processes, mainly LPBF, Binder Jetting (BJ), and Direct Energy Deposition (DED) [112]. Steels of the 300 series are characterised as Ni-Cr steels, with the "L" indicating a low carbon content, specifically below 0.03% of carbon, so AISI 316L stainless steel is a Ni-Cr steel containing a maximum of 0.03% carbon [130, 131]. The complete chemical composition of this steel is available in Table 1.

Table 1: AISI 316L chemical composition [131, 132].

Steel	C (%)	Mn (%)	Si (%)	P (%)	S (%)	Cr (%)	Ni (%)	Mo (%)
AISI 316L	0.030	2.00	1.00	0.045	0.030	16.0 – 18.0	10.0 – 14.0	2.00 – 3.00

PLA was also used to produce the optimised components at a higher scale through FFF.

3.2 Modelling of the Base Components

This master's dissertation focuses on the piston, connecting rod, and the base piston pin. Before concentrating on the topologically optimised piston and connecting rod, their respective base models were first modelled to serve as a comparison. For modelling, optimisation and then assembling, the SIEMENS NX software was used.

3.2.1 Base Piston Modelling

The modelling of the base piston began with its side profile, shown in Figure 20, where it presents a maximum radius of 41 mm, a minimum interior radius of 32.25 mm, and a height of 76.5 mm.

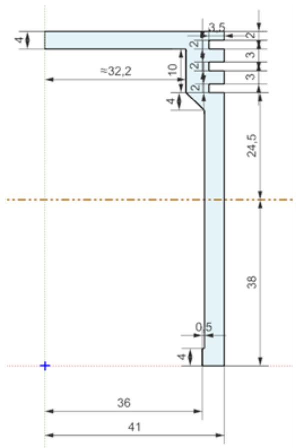

Figure 20: Definition of the piston's side profile dimensions.

After creating the side sketch, the revolve function was used, resulting in a cylindrical body. Then, two holes with a diameter of 20 mm were drilled into the component's frontal face, as seen in Figure 21, to allow the insertion of the piston pin.

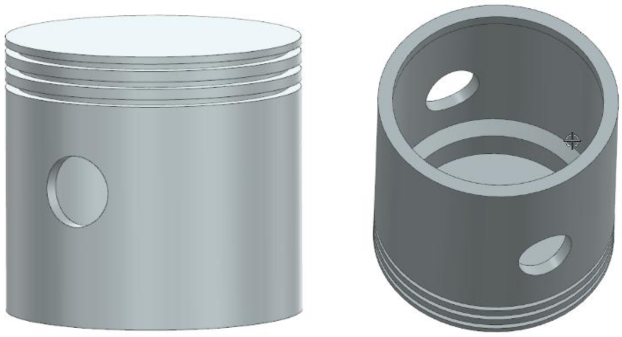

Figure 21: Integration of holes into the piston.

In order to reinforce the interior of the previously drilled hole, it was first required to create a new Datum Coordinate System (DCS) at the centre of the 20 mm circumference, allowing a new datum plane to be established. In this plane, two circumferences with diameters of 20 and 28 mm were sketched, and the area between them was extruded to a distance of 16.3 mm. Afterwards, this feature was mirrored for the other hole, resulting in the model of the base piston seen in Figure 22.

Figure 22: 3D model of the base piston.

3.2.2 Connecting Rod

The modelling of the base connecting rod initiated with the sketch of its front profile, as seen in Figure 23, presenting a distance of 191 mm between the centre of the lower half's circumference and the centre of the upper section. Other relevant dimensions for the base connecting rod were defined, including an inner diameter of 40 mm and an outer diameter of 54 mm for the lower half circumference, and an inner diameter of 20 mm and an outer diameter of 36 mm for the upper section.

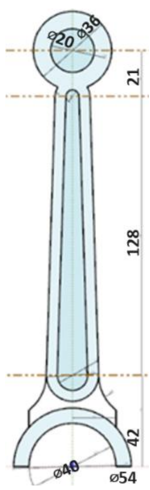

Figure 23: Sketch from the front profile of the connecting rod.

From the previous sketch, various extrusions were created from the bottom to the top. The first extruded area was the lower half circumference, extruded by 36 mm. The next area extruded was directly above it with an extrusion value of 20 mm. Additionally, the centre of the base connecting rod was extruded by 8 mm for the central interior part and 14 mm for the central exterior part. Finally, the upper section was extruded by 18 mm, and all of the extruded volumes were combined, resulting in the solid shown in Figure 24.

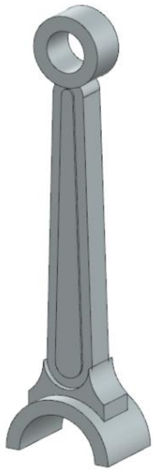

Figure 24: Initial model of the base connecting rod.

To model the lower section of the connecting rod for bolt entry, a new DCS was created. A 20 mm diameter circumference was sketched and extruded by 4 mm, as shown in Figure 25 (a). At its centre, a circumference with a diameter of 18 mm was extruded by 8 mm, as seen in Figure 25 (b). Afterwards, an additional 20 mm circumference was extruded by 4 mm, as displayed in Figure 25 (c). To finalise this section, a 10 mm diameter hole was drilled through all the previous extrusions, as shown in Figure 25 (d).

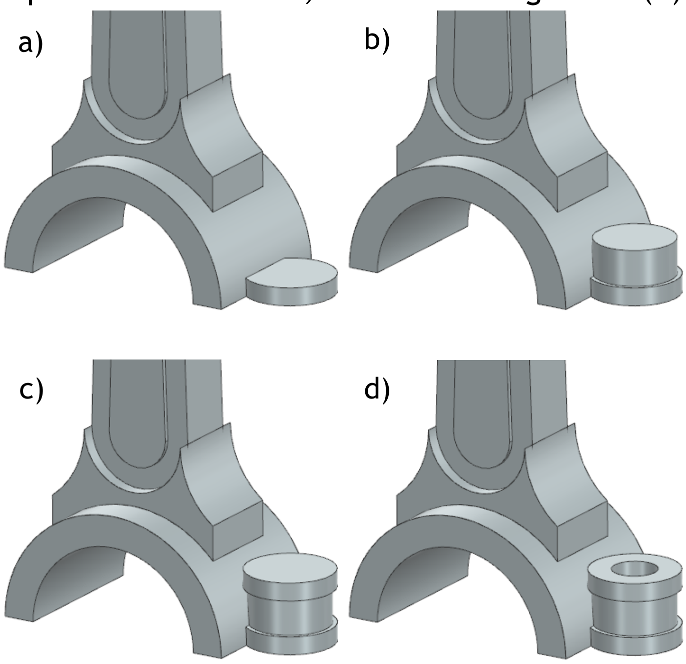

Figure 25: Modelling of the lower section of the base connecting rod: (a) Extrusion of the first circumference; (b) Extrusion of the second circumference; (c) Extrusion of the third circumference; (d) Hole drilled through all the circumferences.

To bring the connecting rod to completion, all these features were mirrored, obtaining the finished 3D model of the base connecting rod, visualised in Figure 26.

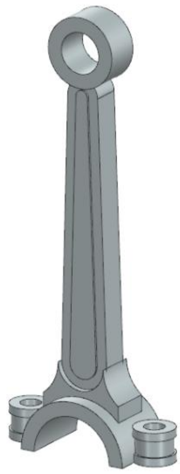

Figure 26: Final 3D model of the base connecting rod

3.3 Topological Optimisation

3.3.1 Optimised Piston

Before obtaining the optimised piston, it was necessary to model the corresponding design space. The previous side sketch of the piston, Figure 20, was taken into consideration, respecting the dimensions for the piston rings, the radius of 41 mm, and the height of 76.5 mm, although some alterations were made, as shown in Figure 27.

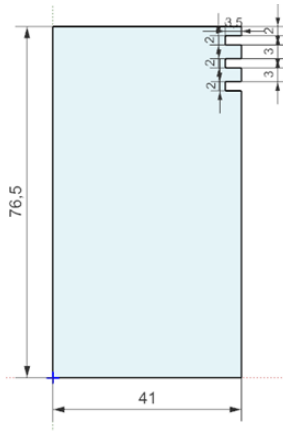

Figure 27: Side profile sketch of the optimised piston design space.

Afterwards, the revolve function was applied to the previous sketch, resulting in the design space of the piston head, illustrated in Figure 28.

Figure 28: Optimised piston design space.

Then, as mentioned earlier, to carry out an effective topological optimisation, it is required to model essential regions of the piston that must be preserved, excluded, or have the shell function applied during the optimisation process. In this chapter, only one construction body will be presented, as it remains unchanged during all the optimised piston iterations. This construction body is specifically a cylinder with a diameter of 20 mm, modelled at the same position where the holes would be, extending through the entire design space, resulting in the solid shown in Figure 29.

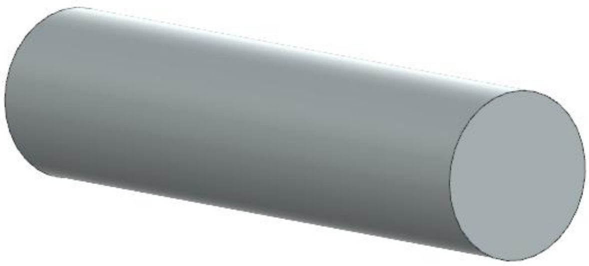

Figure 29: Cylinder with 20 mm diameter.

Further construction bodies are displayed in Chapter 4. After completing all 3D modelling, the topology optimisation was initiated by defining the objective to maximise stiffness and assigning the resolution. The design space, previously modelled, was specified along with all the required construction bodies. As referenced, additional construction bodies were modelled and assigned a function. The long single cylinder with a 20 mm diameter, Figure 29, was set as “Keep Out” to ensure that no material occupies that volume, allowing for the future insertion of the piston pin.

3.3.2 Optimised Connecting Rod

Like the optimised piston, it was first necessary to model the design space for the optimised connecting rod. The sketch, seen in Figure 30 (a), preserved the essential dimensions of the base connecting rod, featuring a half circumference with a diameter of 54 mm and an upper section with a 36 mm circumference. The two distinct areas seen in the sketch were then extruded to different depths: the lower area to 36 mm and the upper area to 20 mm, resulting in the solid present in Figure 30 (b).

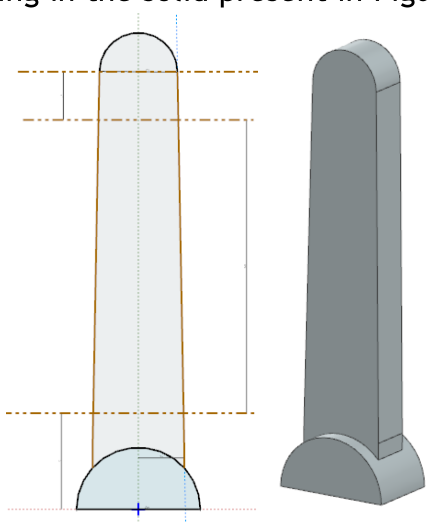

Figure 30: Initial modelling of the design space of the optimised connecting rod: (a) Sketch; (b) Extruded initial body.

To finalise the connecting rod design space, a cylinder with a diameter of 20 mm and a height of 16 mm was extruded, resulting in the solid shown in Figure 31, which represents the design space of the optimised connecting rod.

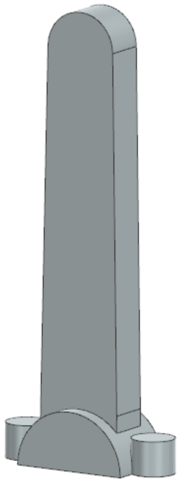

Figure 31: Optimised connecting rod design space.

Then, as was already done for the piston, it was required to model the construction bodies for the topological optimisation, starting with the lower cylinders with a diameter of 10 mm, which were extruded with a height of 16 mm, as seen in Figure 32.

Figure 32: Extruded lower cylinders of the optimised connecting rod.

To create the lower cavity of the optimised connecting rod, it was required to model the solid displayed in Figure 33, which has a diameter of 40 mm and a length of 36 mm.

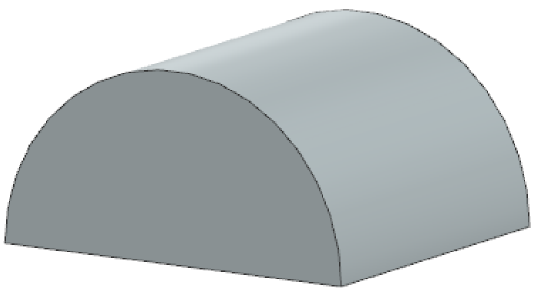

Figure 33: Solid for the lower cavity of the optimised connecting rod.

The last construction body for the optimised connecting rod is a simple cylinder on its upper part with a diameter of 20 mm, which was extruded to 20 mm, as shown in Figure 34.

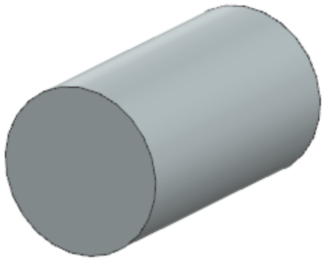

Figure 34: Upper cylinder used as a construction body for the optimised connecting rod.

Succeeding the modelling of the construction bodies for the optimised connecting rod, the topology optimisation was initiated with the same objective as before, to maximise stiffness. Afterwards, the former modelled solids were defined accordingly as the design space and construction bodies. Beginning with the two cylinders seen in Figure 32, the “Shell” function was applied with a value of 2 mm to guarantee clearance for a bolt. The same function with the same value was also used for the half cylinder (Figure 33) and the upper cylinder (Figure 34), to fit onto the crankshaft and to permit access for the piston pin, respectively.

3.4 Environmental Study

In order to determine whether the optimised piston and connecting rod have lower environmental impacts than the standard components, a life cycle analysis was conducted, considering every stage of each component, namely material extraction, production, usage, disposal, and all transportation occurring within and between each stage.

For this purpose, Granta EduPack 2024 R2 was used, where two analyses were performed for each component, resulting in a total of four distinct studies. The specific criteria for each component were applied across every previously mentioned stage. This makes it possible to compare the initial with the optimised component in terms of embodied energy and CO_2 emissions, revealing which component displays a lower overall environmental impact, as will be shown later in Chapter 4.

3.5 Preparation for Additive Manufacturing

After assembling the desired components, the software Materialise was used to define the appropriate scale, position, and set the LPBF parameters. Then, the file was sent to the LPBF machine, initiating the AISI 316L AM process. The specific LPBF machine used was the Prima Additive Print Sharp 150, as shown in Figure 35.

Figure 35: LPBF machine used.

In the case of the FFF, the Bambu Lab software was used, following the same philosophy as the previous one, but applied to the polymer-based FFF process, specifically PLA. In this software, supports were generated, and all the parameters were defined. The file was then sent to the Bambu printer to begin production.

4 RESULTS PRESENTATION AND DISCUSSION

4.1 Topological Optimisation

4.1.1 Optimised Piston

Before initiating the piston topology optimisation, additional construction bodies were needed. A cylinder with a diameter of 36 mm and a total height of 48 mm, as seen in Figure 36, was added to the lower part of the piston to ensure an opening in this section. For this solid, the “Keep out” function was set, ensuring that the volume remains free of material, thereby enabling future access for the connecting rod and allowing both components to be assembled.

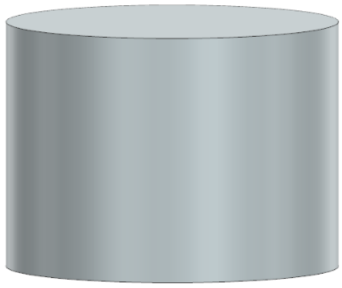

Figure 36: Lower cylinder construction body for the piston optimisation.

Then, another construction body was the upper part of the piston, which was separately remodelled, as shown in Figure 37. The function “Keep In” was applied to this part to preserve the flat surface of the piston and the corresponding gaps for the piston rings.

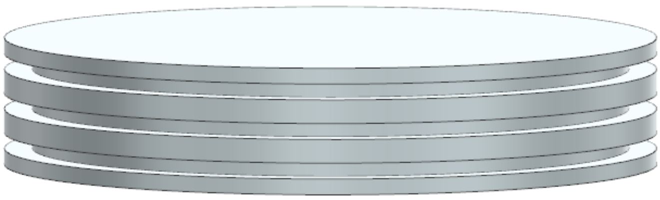

Figure 37: Remodelled upper part of the piston.

After defining the design space and all construction bodies, a maximum mass limit of 0.80 kg was applied, and the minimal resolution was utilised to obtain the first result quickly. Finally, the last step before starting the topological optimisation was to insert constraints and loads. The constraints used were intended to fix the volume that, in real life, would remain stationary, therefore both faces of the long cylinder were fixed, as seen in Figure 38.

Figure 38: Location of the fixed faces.

The loads were applied to the superior flat surface of the piston, with a force of 40800 N, as used in previous case studies [40]. This force was also applied in the opposite direction with the same value, as seen in Figure 39.

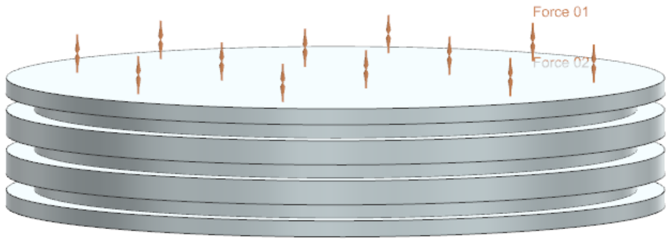

Figure 39: Location and orientation of the applied forces.

With all these criteria and parameters set, the topological optimisation of the piston was started, and the first result is presented in Figure 40. Analysing these results, the absence of a rigid structure around the lateral holes of the piston is noticeable.

Figure 40: First topologically optimised piston obtained.

So, in order to counteract the absence of the rigid structure mentioned earlier, this section was stiffened by adding an inner circumference with a diameter of 20 mm and an outer circumference with a diameter of 28 mm. This sketch was then extruded by 16.3 mm and mirrored, resulting in the solids exhibited in Figure 41. These solids were set as "Keep In" to guarantee that, this time, the optimised piston features a thicker section at the piston pin entrance.

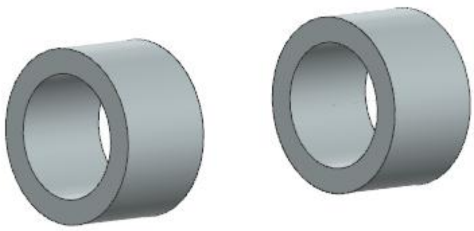

Figure 41: Extruded and mirror solids for the lateral section of the piston.

Following the last alteration, it was required to modify the lower cylinder, reducing its height from 48 to 24 mm. After these modifications, a new optimisation was run, resulting in the second optimised piston, shown in Figure 42.

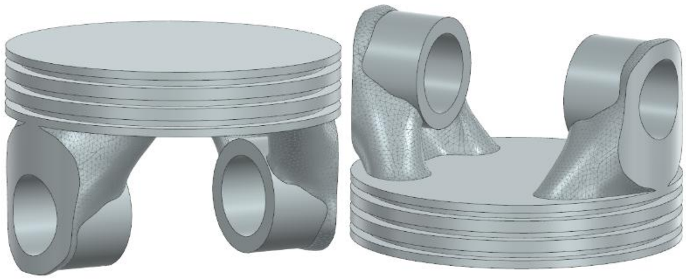

Figure 42: Second version of the optimised piston.

To reduce the piston’s weight, an alteration was made to the remodelled upper part of the piston, Figure 37, which consisted of creating a cavity inside it, as seen in Figure 43, which has a width of 5 mm between the outer and inner circumferences.

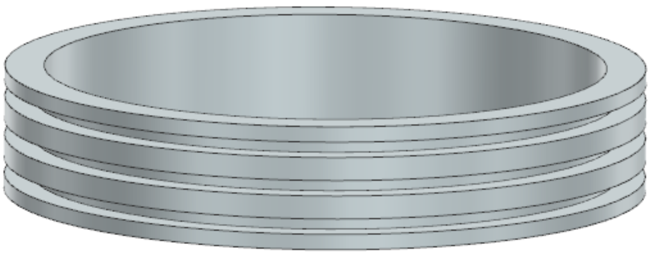

Figure 43: Cavity added to the interior of the remodelled upper part of the piston.

Furthermore, for the third topological optimisation of the piston, the maximum mass limit was reduced to 0.7 kg, and then the optimisation was run, resulting in the third optimised piston observed in Figure 44. This optimised version of the piston allows the arms to extend further into the interior of the upper section.

Figure 44: Third version of the optimised piston.

The third optimised piston iteration resulted in a good design, since, with all the forces applied, it presents a maximum displacement of only 0.0382 mm, as illustrated in Figure 45.

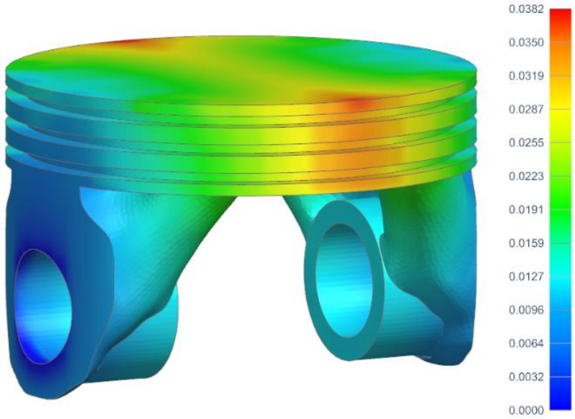

Figure 45: Displacements on the third version of the optimised piston.

Considering the excellent results of the third optimised piston, the construction bodies and the low resolution were kept the same, while the maximum mass limit was reduced to 0.45 kg. Following this adjustment, a new topological optimisation was run, generating the fourth optimised piston shown in Figure 46.

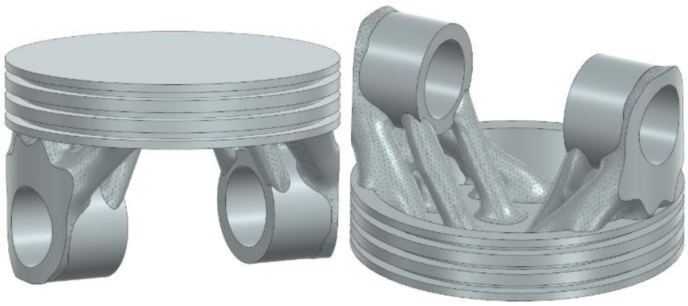

Figure 46: Fourth version of the optimised piston.

In the fourth version of the optimised piston, when compared with the third version (Figure 44), it is possible to observe that the previous dense arms were transformed into a ramifications resembling a tree. This transformation enables a reduction in the piston weight, despite the maximum displacement having more than doubled, reaching a limit value of 0.1068 mm, as seen in Figure 47.

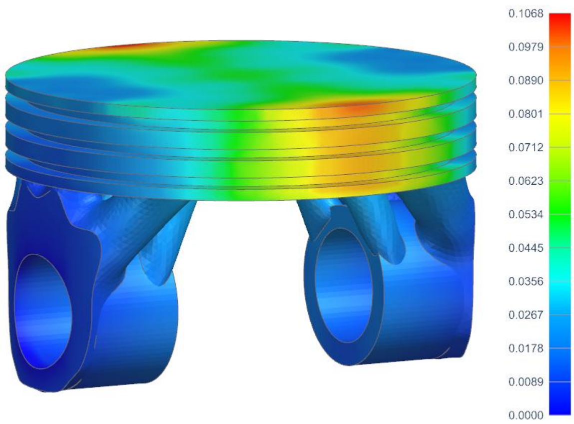

Figure 47: Displacements on the fourth version of the optimised piston.

Even though the maximum displacement is still low, new versions of the optimised piston were tested to achieve a lower value. This time, an alteration was made to the construction bodies, specifically to the solids in Figure 41. Instead of setting them as “Keep in”, they were defined as “Shell” with a value of 4 mm, resulting in a similar geometry of the fourth version of the optimised piston, with a slightly lower maximum displacement of 0.1052 mm, as demonstrated in Figure 48.

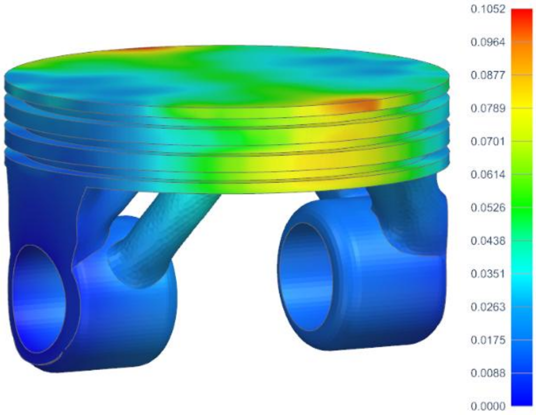

Figure 48: Displacements on the fifth version of the optimised piston.

Maintaining the same approach, a new topological optimisation of the piston was carried out, with the only change being a reduction of the “Shell” value from 4 to 3 mm. This simple alteration resulted in a marginal improvement in the maximum displacement, achieving a limit value of 0.0965 mm, as displayed in Figure 49.

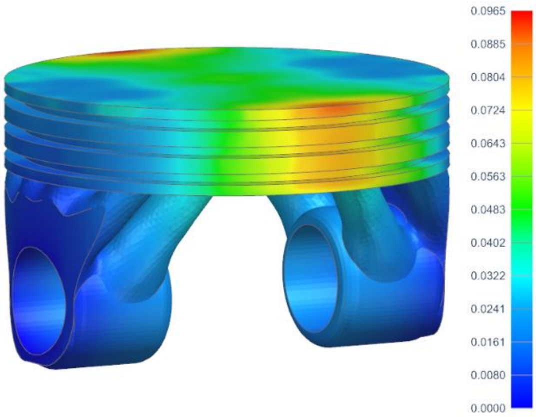

Figure 49: Displacements on the sixth version of the optimised piston.

With the great results of the sixth optimised piston (Figure 49), the resolution was increased, leading to minor alterations in the geometry and a considerable reduction in the maximum displacement to 0.0800 mm, as portrayed in Figure 50.

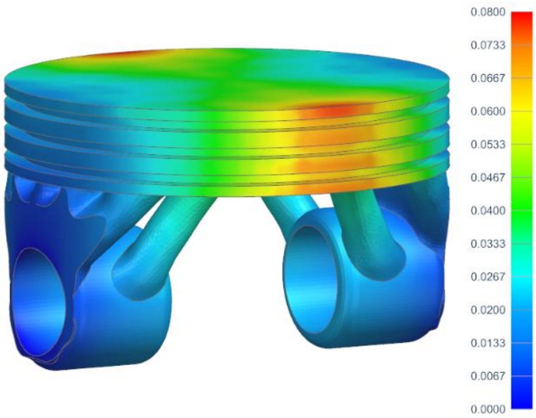

Figure 50: Displacements on the seventh version of the optimised piston.

The two best results of the piston optimisation are the third (Figure 45) and the seventh (Figure 50) versions. The third iteration offers a lower maximum displacement of 0.0382

mm, compared to the 0.0800 mm obtained in the seventh. Although the final optimisation exhibits a higher maximum displacement, it is significantly lighter, being 36% lighter than the third version. This is a major advantage, as it reduces the environmental impact both during the component's lifetime and in terms of material usage, as it will be discussed further in this chapter. Considering this, it compensates for the increased maximum displacements, which remain relatively low. In summary, the seventh optimisation is the best option, since it achieves a considerably low maximum displacement while maintaining a reduced mass of 0.45 kg.
While the seventh piston iteration (Figure 50) presented the best result, it still requires one geometric alteration: a more cylindrical entrance for the piston pin. To achieve this, the area between two circumferences, one with a diameter of 26 mm and the other with a diameter of 20 mm, was extruded to the virtual extension of the face and then mirrored, resulting in the final version of the optimised piston, displayed in Figure 51.

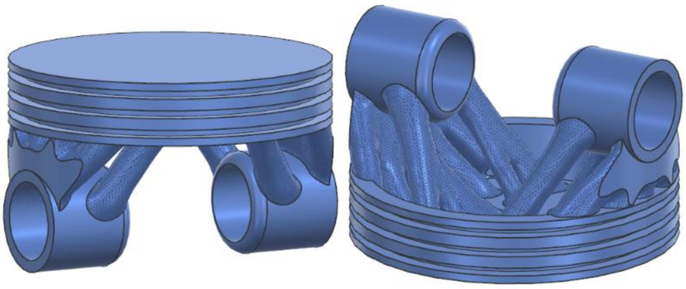

Figure 51: Final version of the optimised piston.

4.1.2 Optimised Connecting Rod

To initiate the "Topology Optimisation" tab, just like for the optimised piston, the first step is to define the desired resolution and the objective, which is to maximise stiffness. In this initial version, the resolution was set to the minimum value to prioritise a faster optimisation result. Then, the previously modelled construction bodies and design space were used and defined accordingly. Afterwards, just as with the piston optimisation, it was necessary to set the constraints and loads. Furthermore, the maximum mass limit was set at 0.3 kg, followed by the areas where the entire 3D model was fixed, as displayed in Figure 52, and the directions/values of the forces applied during the simulation.

Figure 52: Fixed positions for the topology optimisation of the connecting rod.
For the first optimisation, vertical forces of just 1 N were applied to the upper cylinder in order to quickly test the resulting optimised geometry, as seen in Figure 53.

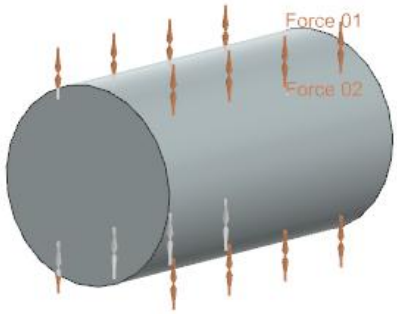

Figure 53: Vertical forces applied to the upper cylinder.

After defining all these parameters, the first topological optimisation was run, resulting in the optimised connecting rod shown in Figure 54.

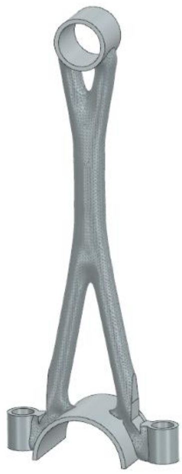

Figure 54: First version of the optimised connecting rod.

Following the first optimisation, the lowest value allowed for the maximum mass limit was tested, which was 0.189 kg. Aside from this change, the design space, all construction bodies, constraints, and loads remained the same, generating the second optimised connecting rod, as seen in Figure 55.

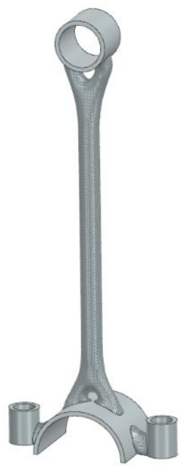

Figure 55: Second version of the optimised connecting rod.

Comparing the first two optimisations of the connecting rod, it was noticed that due to a higher mass, the initial optimisation (Figure 54) presents a thicker middle section than the second optimisation (Figure 55), enabling it to withstand greater forces with lower maximum displacements. Furthermore, the first version of the optimised connecting rod is slightly more complex. Considering the mass difference between the two is practically 100 g, it was decided that the first optimised connecting rod would serve as the starting point. Afterwards, a study was conducted to examine the effect of the resolution, using both medium and maximum resolutions as displayed in Figure 56. From the minimum resolution used in Figure 54 to the medium and maximum resolution shown in Figure 56, it is noticeable that increasing the resolution results in a more refined geometry with a smaller intersection area between the left and right sections of the optimised connecting rod. Additionally, a higher resolution also leads to the formation of more arms linked to the lower half circumference of the connecting rod.

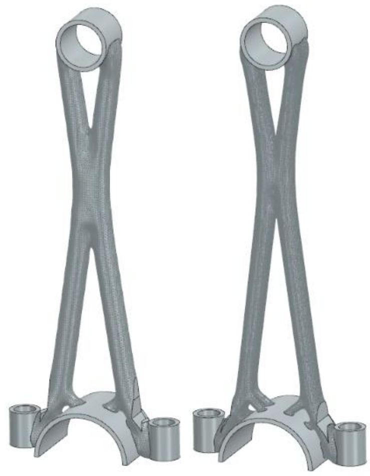

Figure 56: Optimised connecting rods with medium resolution (left) and maximum resolution (right).

For the next optimisation, diagonal forces were defined to more accurately simulate the direction of the forces during combustion. However, for this optimisation, a force of 1 N and a minimum resolution were defined to accelerate the topological optimisation while still obtaining a coherent result. To define these forces, it was initially required to create a new DCS at the centre of the upper cylinder, which allowed the creation of a datum plane angled at 30 º relative to the Z-axis. This plane was then mirrored, permitting the application of both forces on these planes, resulting in a total of four forces applied to the upper cylinder, as seen in Figure 57.

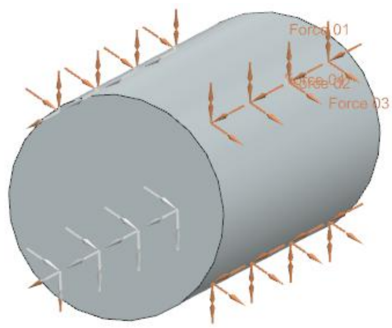

Figure 57: Vertical and diagonal forces applied to the upper cylinder.

After the addition of the previously mentioned forces, the topological optimisation was initiated, generating the fifth optimised connecting rod present in Figure 58.

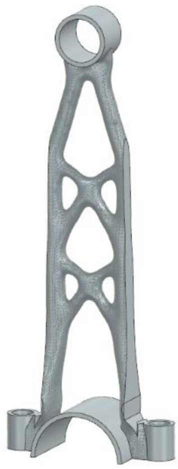

Figure 58: Fifth version of the optimised connecting rod.

Relative to the first optimised connecting rod (Figure 54), the fifth version (Figure 58) exhibits a more complex geometry, resulting from the addition of more forces in different orientations. This latest optimisation displays intricate arms intersecting at the centre, forming two zones that result from the union of four arms. Given the interesting geometry obtained in this optimised connecting rod, a new optimisation was started with the same parameters as the fifth version, changing only the resolution. This generated a highly complex geometry as displayed in Figure 59.

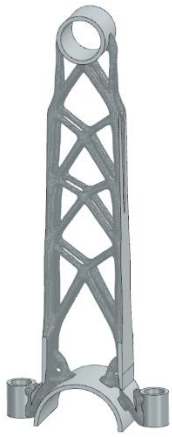

Figure 59: Sixth version of the optimised connecting rod.

Relative to the fifth optimised connecting rod (Figure 58), this latest version (Figure 59) presents a total of six intersections at the centre of the component. Furthermore, it possesses two arms, one on each side, connected to the upper circumference, and additional arms joined to the lower half circumference. In light of the previous outcome, a new optimisation was performed using the real values of the forces. As with the optimised piston, the vertical forces have a value of 40800 N. However, diagonal forces had to be calculated, resulting in a value of 23556 N, obtained through Equation 3.

$$40800 * tan(30) = 23556\ N \tag{3}$$

With these alterations to the force values, a new topological optimisation was run, resulting in a new optimised connecting rod with the same geometry as the prior version (Figure 59). With this new version, it is possible to analyse the displacements experienced by the connecting rod during the application of forces, as represented in Figure 60. This iteration of the optimised connecting rod had a maximum displacement of 0.873 mm on the upper cylinder, and the largest displacements occur in the zones closest to it, gradually decreasing along the height of the connecting rod.

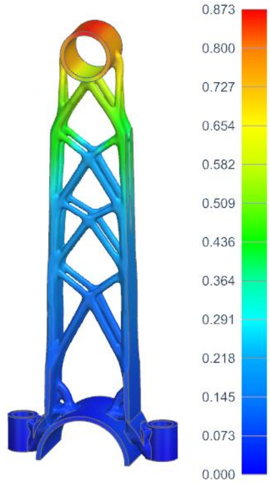

Figure 60: Displacements on the seventh version of the optimised connecting rod.

To improve the maximum displacement value of this latest version of the optimised connecting rod, a thicker volume linked to the upper cylinder had to be modelled. To achieve this, a new datum plane was initially created at the centre of the right upper arm, which is interconnected with the upper cylinder. A circumference with a diameter of 12 mm was sketched on this plane and then extruded until the upper cylinder, as shown in Figure 61 (a). Using these extruded sections, a new Datum Plane was created 2 mm away, on which a 6 mm diameter circumference was sketched. With these two circumferences defined, the “Swept” function was applied, generating the feature seen in Figure 61 (b). Afterwards, a curved line was centred on the 6 mm diameter circumference. At the end of this line, another datum plane was created, allowing a 2 mm diameter circumference to be sketched. The “Swept” function was then used between the 6 mm and the 2 mm circumferences, utilising the prior line as a guide, to create the solid curve shown in Figure 61 (c). Another 2 mm diameter circumference was sketched in the same direction as the previous one and extruded, as seen in Figure 61 (d). Finally, a small circumference was sketched inside the optimised arm, and the “Swept” function was selected again, using this and the last 2 mm diameter circumferences as the “Sections” and the curve at the centre of both circumferences as “Guide”. This final addition is illustrated in Figure 61 (e).

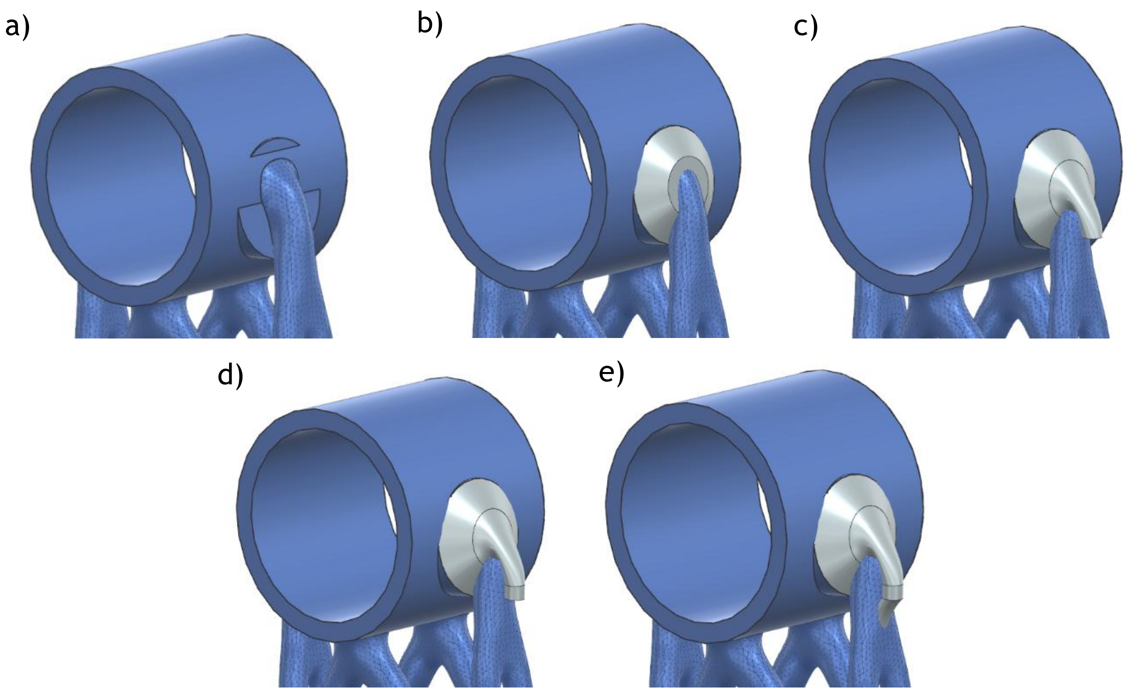

Figure 61: Evolution of the reinforcement for the upper cylinder: (a) Extrusion of the 12 mm diameter circumference; (b) Feature resulting from the swept function between the 12 mm and 6 mm circumferences; (c) Feature resulting from the swept function between the 6 mm and 2 mm circumferences; (d) Extrusion of another 2 mm diameter circumference; (e) Feature resulting from the final swept function.

To conclude the reinforcement of the upper cylinder, all the previous sections were united and then mirrored, resulting in the upper reinforcements seen in Figure 62.

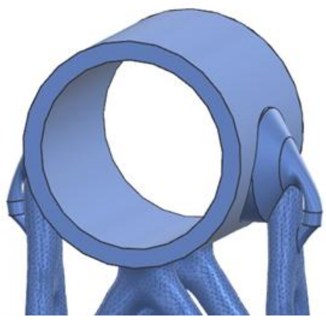

Figure 62: Reinforcement of the upper cylinder.

Further adjustments were made to the geometry of the connecting rod, specifically to the gaps near the half circumference and the two lower cylinders, as seen in Figure 63.

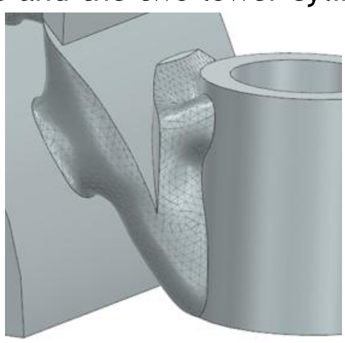

Figure 63: Gap on the lower part of the connecting rod.

In order to solve this gap, the outer curve was first selected and then extruded using the "Until Extended" option, meaning that this curve is extruded until it encounters a boundary, resulting in the feature seen in Figure 64 (a). Next, a small half circle was sketched and then extruded, applying the same option as before. However, as can be analysed in Figure 64 (b), this half circumference was not aligned with the prior extrusion. To resolve this issue, additional extrusions were performed until the final geometry was achieved, as displayed in Figure 64 (c).

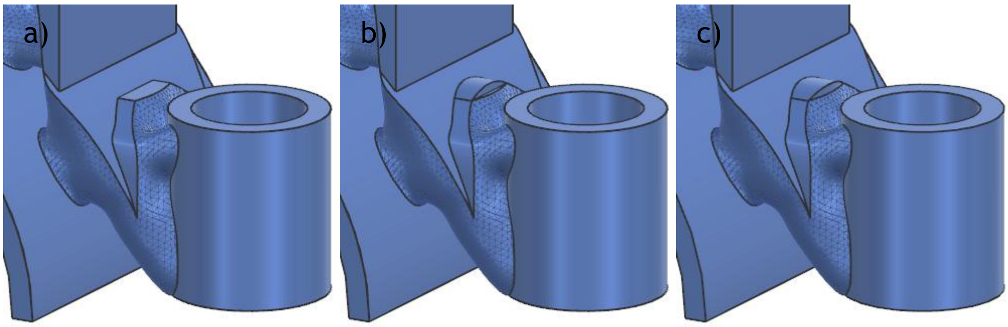

Figure 64: Evolution of the correction of the gap in the lower part of the connecting rod: (a) Curve extended; (b) Half circumference; (c) Final geometry of this feature.

Then, all these extrusions were united together, as well as with the connecting rod, and subsequently mirrored so that both sides are symmetrical. The connecting rod after these changes is shown in Figure 65.

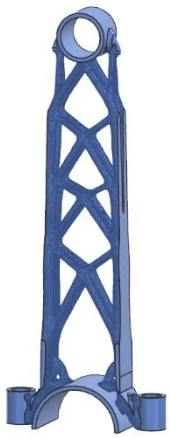

Figure 65: Remodelled seventh optimised connecting rod.

Afterwards, this latest remodelled connecting rod was subjected to another topological optimisation. The parameters were essentially the same as those used in the seventh version (Figure 60), with the addition of two shape constraints: planar symmetry constraints to ensure that the connecting rod remained symmetrical in frontal and lateral planes. A new optimisation was then run using maximum resolution, generating the eight optimised connecting rod. It was analysed in terms of displacement, showing a maximum displacement of 0.791 mm located, as expected, in the upper part of the connecting rod and gradually decreasing along the distance to the upper cylinder, as seen in Figure 66.

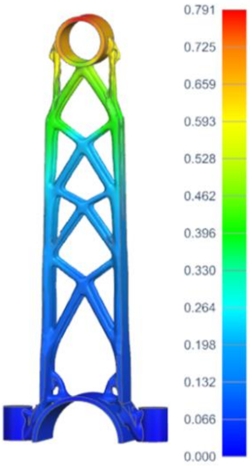

Figure 66: Displacements on the eighth version of the optimised connecting rod.

Comparing the seventh (Figure 60) and eighth (Figure 66) versions of the optimised connecting rod, a slight reduction in the maximum displacement from 0.873 to 0.791 mm is noticeable. This decrease indicates that the reinforcement in the upper part was effective, although it is still insufficient, since the maximum displacement remains relatively high. Geometrically, the eighth version presents some alterations to the initial design space, most notably in the previously modelled upper reinforcement, which underwent some modifications, as displayed in Figure 67.

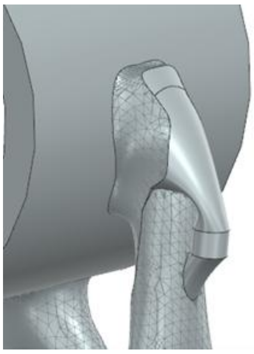

Figure 67: Optimised reinforcement for the upper cylinder.

Other slight modifications also occurred in the eighth version, where some arms were thinner than in the seventh version. Considering that the modifications made to the seventh version must have increased the weight of the component, a new optimisation was carried out, maintaining all the parameters except for the maximum mass limit, which was changed from 0.3 to 0.5 kg. After the optimisation was run, a displacement study indicated a maximum value of 0.427 mm, and the resulting geometry was essentially the same as the remodelled design space, with both factors visible in Figure 68.

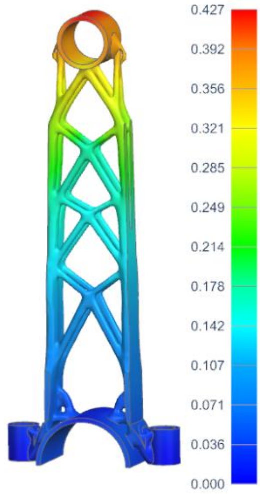

Figure 68: Displacements on the ninth version of the optimised connecting rod.

In comparison, the maximum displacement of the ninth version (Figure 68) is considerably lower than the 0.791 mm observed on the eighth version (Figure 66). However, the ninth optimised connecting rod exhibits higher displacement values farther from the upper cylinder, as indicated by a larger area in light blue. This suggests that displacements in these sections exceed 0.142 mm, whereas in the eighth version, the dark blue areas are more prominent than the light blue ones.

The eighth optimised connecting rod (Figure 66) was chosen for further improvement due to its lower weight and fewer sections affected by the applied forces, exhibiting lower or even no displacements compared to the ninth version (Figure 68). Based on this, the eighth optimised connecting rod was remodelled to achieve a more significant reduction in maximum displacement.

To begin with, the small gap between the upper reinforcement and the optimised arm, as seen in Figure 69 (a), was eliminated by adding a cylinder with a diameter of 5 mm and an extrusion length of 13 mm, Figure 69 (b). A new datum plane, and subsequently a new sketching plane, were created where a circumference of 8 mm was drawn. A line was then sketched between the centres of the 5 and 8 mm circumferences, enabling the use of the “Swept” function, which was mirrored to produce the geometrical alterations seen in Figure 69 (c). To properly connect these new features to the optimised body, an additional 5 mm diameter circumference and a line connecting it to the previous 8 mm circumferences were created. Using the “Swept” function, a subtle design alteration was created, as displayed in Figure 69 (d), which was then mirrored to maintain symmetry. With this section enlarged, the areas directly beneath the connection rod were also widened to better withstand the applied forces. To accomplish this objective, an 8 mm circumference was sketched and extruded up to the extension of the desired face. The next step involved applying the “Swept” function between this recently sketched circumference and the previous 8 mm circumference located lower on the arm. This was mirrored, causing the central arms to widen, as shown in Figure 69 (e). Finally, all the prior modelled features were mirrored across both symmetry planes and unified, completing the reinforcement of the upper arms adjacent to the upper cylinder, as seen in Figure 69 (f).

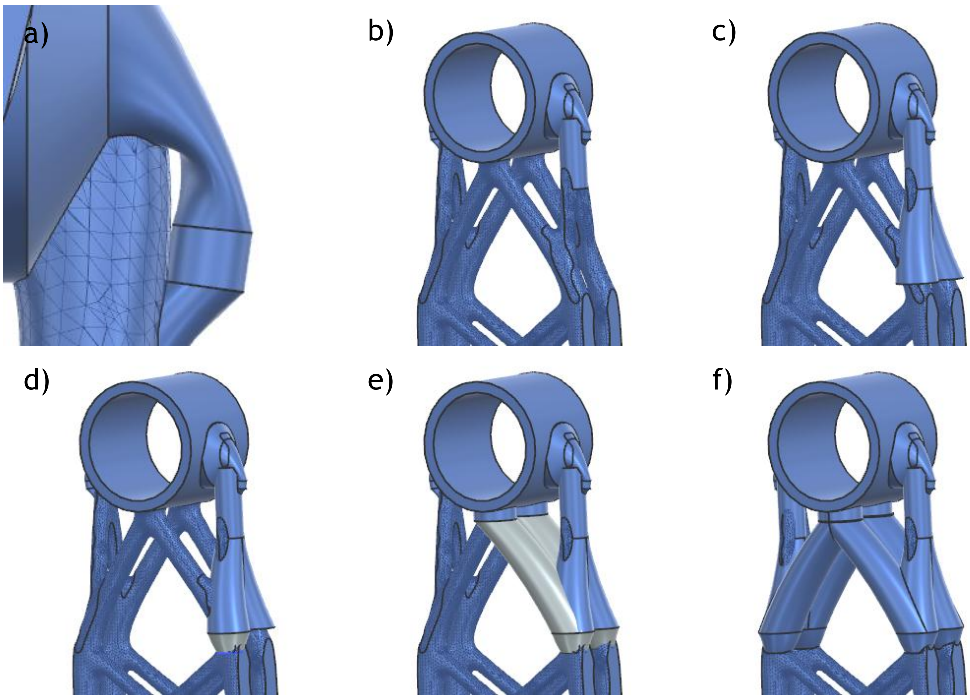

Figure 69: Evolution of the widening of the arms near the upper cylinder: (a) Initial gap; (b) First extruded cylinder; (c) Alterations after first Swept and mirrored features; (d) Subtle detail; (e) Wider central arms; (f) Symmetric upper section of the reinforced optimised connecting rod.

After these alterations to the arms near the upper cylinder, a new topological optimisation was run using the same parameters as the eighth optimisation, which were to maximise stiffness, use maximum resolution, the same construction bodies as before, two planar symmetry constraints, a maximum mass limit of 0.3 kg, the other constraints and loads previously mentioned. Once all parameters were defined, the tenth optimisation was initiated, resulting in a poor outcome with a maximum displacement of 10.796 mm, as seen in Figure 70.

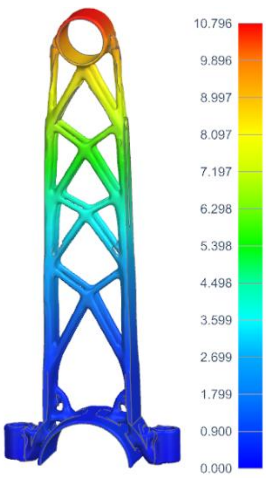

Figure 70: Displacements on the tenth version of the optimised connecting rod.

Furthermore, the tenth optimisation also displays some geometrical inconsistencies, particularly in the arms that are laterally closest to the upper cylinder, where it is evident that the previously added reinforcement does not connect well to the rest of the optimised body, as seen in Figure 71 (a). The upper cylinder itself also fails to comply with the 2 mm “Shell” restriction, displaying a thinner opening with some superficial defects as shown in Figure 71 (b). These defects are also clearly visible in the lower and half cylinders, where all of them show a lack of material, as can be seen in Figure 71 (c).

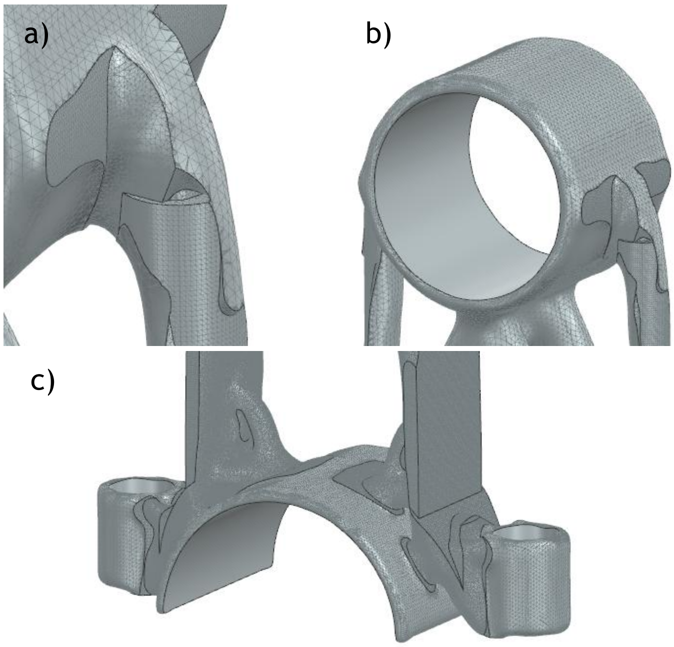

Figure 71: Defects observed in the tenth optimisation of the connecting rod: (a) In the arm close to the upper cylinder; (b) In the upper cylinder itself; (c) In the lower part.

Due to the bad results of the tenth connecting rod optimisation, the previous reinforcements added to the solid were either modified or removed. The new adjustments to the eighth optimisation of the connecting rod, Figure 66, began with increasing the diameter of the circumference surrounding the upper arm, before it splits, to 10 mm and extruding it by 8 mm, as shown in Figure 72 (a). Afterwards, the lower modifications previously made were reused, such as the lower circumference of 8 mm, which enabled the application of the "Swept" function. This generated a thicker arm than in the prior version, as can be seen in Figure 72 (b). Next, the exact lower section of the earlier reinforcement was reused, and both implementations were mirrored, producing the adaptations seen in Figure 72 (c). The reinforced central arms were also reutilised and united with the newly implemented features, resulting in the geometry displayed Figure 72 (d). To create a smoother connection between the reinforced arms and the upper cylinder, reducing the risk of increased displacement values, a small circumference was sketched, and, as usual, a line connecting its centre to the 10 mm circumference was drawn. The "Swept" function was applied, creating a smooth and larger contact area with the upper cylinder, which should contribute to lowering the maximum displacement value. Finally, one last "Swept" operation was performed to complete the smooth connection to the upper cylinder. All these features were then mirrored and united, resulting in the final version of the upper reinforcements, as illustrated in Figure 72 (e).

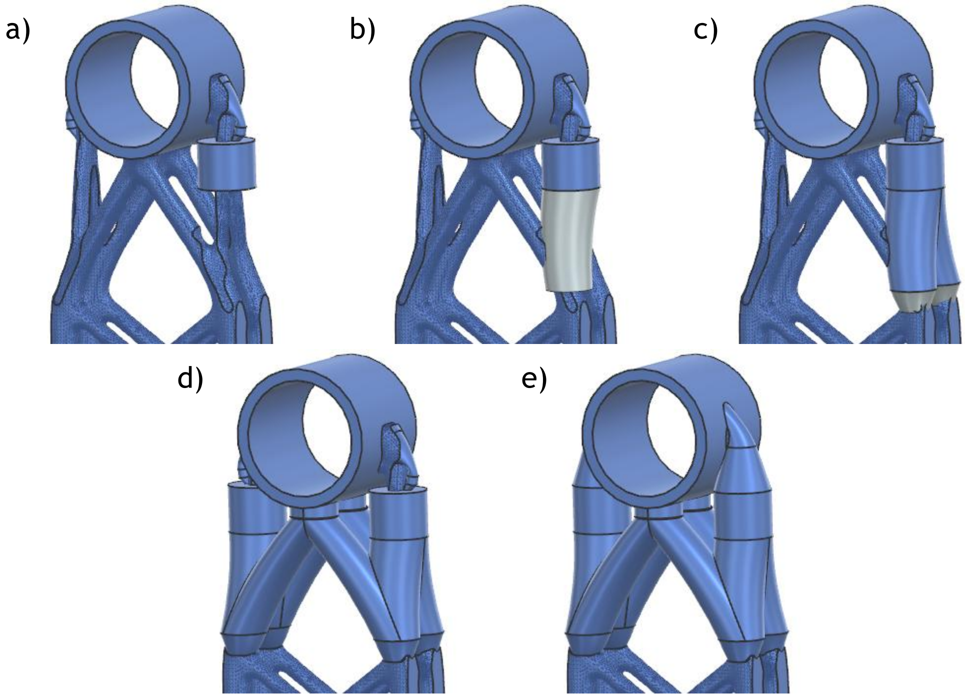

Figure 72: Evolution of a smoother widening of the arms closer to the upper cylinder: (a) First extruded cylinder; (b) Reinforced lateral arm; (c) Subtle swept solid, (d) Reinforced central arms; (e) Smooth connection to the upper cylinder and mirrored features.

When these alterations were concluded, a new optimisation was initiated with the maximum resolution and the same objective, construction bodies, constraints and loads as the most recent optimisations. The maximum mass limit was set at 0.3 kg, allowing the generation of the eleventh optimised connecting rod with the lowest maximum displacement value so far, of 0.242 mm. Even when compared with the ninth version (Figure 68), which has a mass of 0.5 kg and a maximum displacement of 0.427 mm, the improvements in this version are even more impressive, having both less weight and nearly half of the maximum displacement. However, the geometry obtained is much simpler, being almost entirely hollow in the interior of the connecting rod. Both the displacements and the geometry of the eleventh optimised connecting rod can be seen in Figure 73.

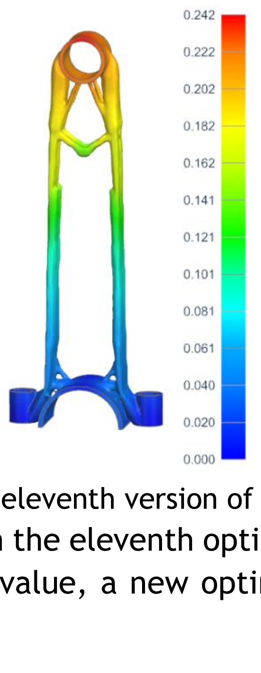

Figure 73: Displacements on the eleventh version of the optimised connecting rod.

To improve the geometry obtained in the eleventh optimisation and, of course, to further reduce the maximum displacement value, a new optimisation was performed using the same parameters as the previous version, except that the maximum mass limit was increased to 0.4 kg. The twelfth version of the optimised connecting rod achieved an even lower maximum displacement value than the eleventh version (Figure 73), reaching 0.215 mm. Although it has the same mass as the ninth version (Figure 68), it shows nearly half the maximum displacement, decreasing from 0.427 mm to 0.215 mm. Furthermore, the geometry of the twelfth version is far more complex than of the eleventh, featuring intricate arms that interconnect at the centre of the connecting rod, which helped to reduce the maximum displacement. Though some ramifications in the lower half circumference and in both lower cylinders present minor geometrical inconsistencies. The displacements and geometry of the twelfth optimisation are shown in Figure 74.

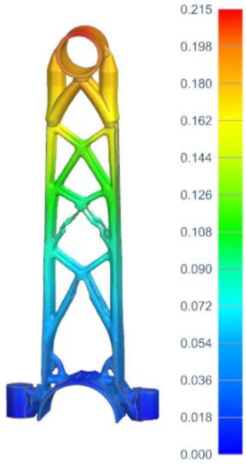

Figure 74: Displacements on the twelfth version of the optimised connecting rod.

A new optimisation was also carried out, this time with a maximum mass limit of 0.5 kg. This optimisation aimed to test whether the previous defects were resolved and also to reduce the maximum displacement value. However, the results of the thirteenth optimised connecting rod were disappointing, since the same maximum displacement value as the twelfth version (Figure 74) was obtained, 0.215 mm. The only advantage this version offers over the previous one is that some of the defects mentioned were resolved. Nevertheless, some issues remain, such as in the right lower cylinder and the half circumference. In Figure 75, the displacements and the geometry of the thirteenth optimisation can be seen.

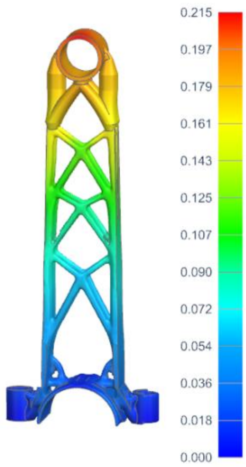

Figure 75: Displacements on the thirteenth version of the optimised connecting rod.

In summary, these three optimisations all presented great results compared to the previous versions, making it possible to affirm that the reinforcements made to the upper cylinder were successful. Considering the points already discussed, the best optimisation of the three is the twelfth version (Figure 74). Although it is not the lightest, it has the lowest maximum displacement value while maintaining an interesting geometry. The thirteenth version (Figure 75) is not worth considering, since it presents the same maximum displacement value, fails to solve all the geometrical inconsistencies, and is heavier.

In order to fix the previously mentioned defects of the twelfth optimisation (Figure 74), some remodelling was carried out, starting with the central arms. Two circumferences were sketched, a lower one with a diameter of 9 mm and an upper one with 5 mm, along with a line connecting the centres of both, allowing the use of the "Swept" function to generate the widened arm displayed in Figure 76 (a). As seen in Figure 76 (a), the "Swept" does not fully cover all the defects in this arm, so further modelling was required using both extrude and sweep functions. Once the defects were completely covered, these additions were united with the prior optimised body as seen in Figure 76 (b). To finalise, the central arm modifications were mirrored in both planes to maintain symmetry and then united with the main body, obtaining the widened central arms shown in Figure 76 (c).

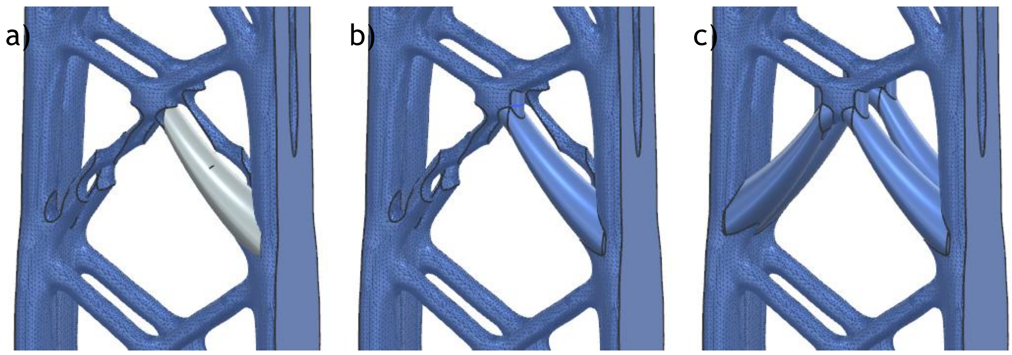

Figure 76: Evolution of the widening of the central arms: (a) Initial widening of one arm; (b) Correction of defects from the previous widening; (c) Mirrored and united widened arms.

The lower central arms also required correction, so the same approach as before was applied. It began with a larger lower circumference of 10.8 mm in diameter, ensuring that the entire lower part of the arm was enclosed, and a smaller upper circumference of 9 mm in diameter. Additionally, an extra circumference with a diameter of 4 mm was sketched inside the central interconnection of four arms. Then, a line passing through the centres of all three circumferences was sketched, and the "Swept" function was used to create the feature shown in Figure 77 (a). The lower part of this thickened arm was smoothed with the "Edge Blend" function, and the resulting geometry was mirrored in both planes and united, producing the modifications seen in Figure 77 (b).

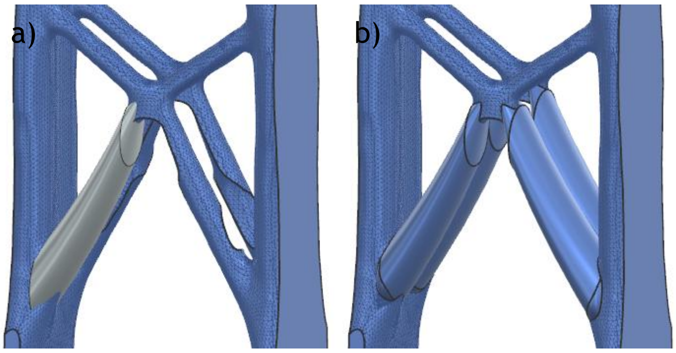

Figure 77: Evolution of the widening of the lower arm: (a) First phase of widening one arm; (b) Final phase of the widening of all lower arms.

To finalise all the modifications required to remove the geometrical inconsistencies, it was necessary to extrude the area between the half circumference and remodel one of the lower cylinders, resulting in a smoother, defect-free geometry as seen in Figure 78.

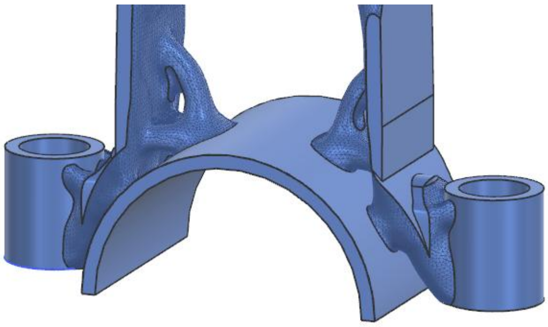

Figure 78: Result of the lower part of the connecting rod after the defect corrections.

Afterwards, a new optimisation was initiated using the same criteria as the one that produced the best results, Figure 74, maintaining a maximum mass limit of 0.4 kg and utilising the maximum resolution. Unfortunately, the results were not better than those obtained in the twelfth optimisation. As can be seen in Figure 79, the maximum displacement of the fourteenth optimised connecting rod is 0.436 mm, which is more than double the value previously achieved.

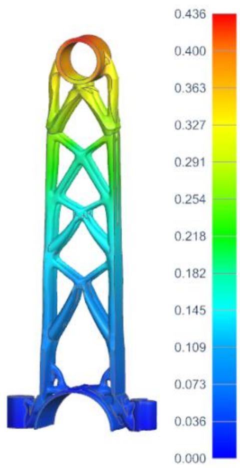

Figure 79: Displacements on the fourteenth version of the optimised connecting rod.

Considering this, the best connecting rod obtained was the remodelled twelfth optimisation, which presents the lowest maximum displacement of 0.215 mm while weighing only 0.4 kg. After the remodelling, it also displays a smooth geometry without inconsistencies. The final version of the connecting rod geometry is shown in Figure 80.

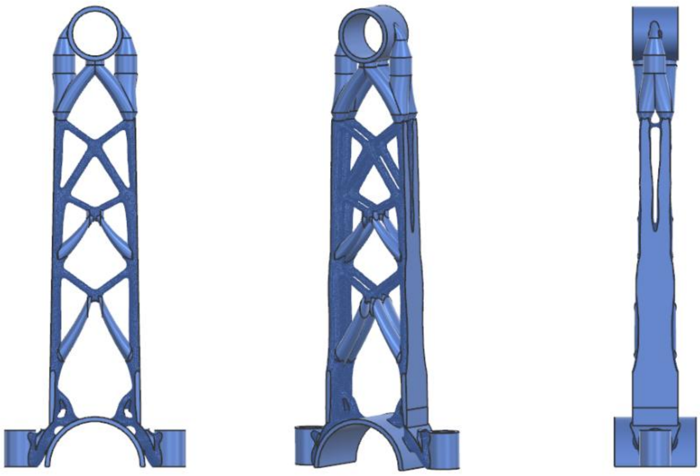

Figure 80: Views of the final version of the optimised connecting rod.

4.2 Comparison between the Base Model and the Optimised Model

In order to make a valid comparison between the base model and the optimised version of the piston and connecting rod, it is necessary to place the base model under the same conditions as the optimised components. For this, the topology optimisation tab for both the base piston and connecting rod were opened to verify their respective masses and apply the forces each component is subjected to. After defining the same conditions as the optimised versions, a displacement study was conducted for each part.

4.2.1 Piston

The mass of the base piston model is 0.884 kg, which is almost double the 0.45 kg of the final optimised version shown in Figure 51. Furthermore, the maximum displacement of the base model is 0.124 mm, being considerably higher than the 0.0800 mm already obtained.

In summary, the results from the optimised piston have shown that it is incredibly successful when compared to the starting point, since it was possible to reduce the weight by 49.10% and the maximum displacement value by 35.48%. This means the component can withstand the same forces with lower displacements while being lighter.

4.2.2 Connecting Rod

The mass of the base connecting rod is 0.586 kg, which is slightly higher than the 0.4 kg of the optimised version. Additionally, the base model also shows a marginally higher maximum displacement value of 0.235 mm, just 0.020 mm more than that of the final optimised connecting rod. These results exhibit that the most significant advantage of the optimised connecting rod is the weight reduction, which amounts to a 31.74% decrease.

Although the results are not as impressive as those achieved with the optimised piston, the reduction in mass while nearly maintaining the same maximum displacement value, with only a reduction of 8.51%, is still positive.

4.3 Environmental Analyses

Before starting the environmental analyses, it is necessary to set some parameters common to both the piston and connecting rod, whether in their initial or optimised versions. These parameters are mostly related to the type of car in which they will be used. Considering that sports cars benefit more from weight reduction in terms of performance, it is essential to analyse how this reduction impacts the environment, regarding embodied energy and CO_2 emissions.

For these analyses, it was established that the type of vehicle is, as previously mentioned, a sports car, which uses petrol as fuel. The lifetime of these components was defined at 10 years, during which the vehicle travels 27.4 km per day for 365 days a year, resulting in a total of 100010 km at the end of its life. Furthermore, the production of 10000 units of each component was considered, all made from the same material, which is the austenitic stainless steel 316L with 0% recycled content. Additionally, both the pistons and connecting rods were assumed to be manufactured in Germany and then transported to Portugal by lorry, where they will be assembled with the rest of the car and used throughout their lifetime. Finally, the end of life was assumed to be the same for each component, consisting of landfill disposal.

4.3.1 Environmental Impact comparison between the Base and Optimised Piston

As previously mentioned, the base piston weighs 0.884 kg. Since it was established that these pistons, both base and optimised, would be used in sports cars, in the case of the base piston, it was assumed to be produced through forging, due to its enhanced performance and properties compared to cast pistons. In order to select the ideal lorry to transport the total weight of these pistons, it was necessary to calculate their total weight using Equation 4.

$$Total\ weight\ =\ Component\ weight * Number\ of\ components \tag{4}$$

Considering that each piston weighs 0.884 kg and, as indicated earlier, the number of components defined was 10000 units, using Equation 4, it is possible to calculate that the total weight of this lot is 8840 kg. After obtaining the total weight, a lorry capable of transporting such a load was selected, which was a 7.5 – 16 t Euro 6 lorry.

Similar to the base piston, the optimised piston uses most of the same parameters, including the lorry, to ensure a valid comparison between the two. However, the weight of the optimised version is lower, at 0.45 kg. Additionally, the production process differs, being LPBF, which requires the inclusion of embodied energy and CO_2 emissions specific to this method. To account for this, the energy consumption for LPBF was set at 152 MJ/kg [133]. Since the software used does not allow the definition of additional parameters in the material stage, the energy required to produce metal powders after extraction was included in the manufacturing stage, where 47 MJ/kg of the 152 MJ/kg were utilised in the stainless steel powder production. Regarding CO_2 equivalent emissions, Baroutaji et al. combined the emissions from material extraction, powder fabrication and component manufacturing, obtaining a value of 25 kg CO_2 equivalent/kg [134, 135]. To include only the powder and component production in the manufacturing stage, Equation 5 was applied to calculate the CO_2 equivalent in kilograms per component produced, resulting in a value of 3.36 kg CO_2/unit.

$$CO_{2-eq} per\ component = \frac{Emissions\ Extraction}{Total\ units}\ kg\ CO_2/un \quad (5)$$

Then, considering that the optimised piston weighs 0.45kg, it was determined that 2.2 units are required to obtain 1 kg of component. Following this, the CO_2 equivalent emissions for the material extraction were calculated using Equation 6, resulting in a total of 7.46 kg CO_2/kg.

$$CO_{2-eq}\ emissions\ from\ Extraction = CO_{2-eq} per\ component * n\ of\ components\ in\ 1\ kg \quad (6)$$

Lastly, the CO_2 equivalent emissions from extraction were subtracted from the previously mentioned 25 kg CO_2 equivalent/kg, obtaining 17.54 kg CO_2 equivalent/kg from powder production and components manufacturing, which falls within the expected range of 13 to 68 kg CO_2 equivalent for the LPBF process using stainless steel [133]. This value was then introduced into the manufacturing stage of the software.

After defining all these parameters and characteristics of the base and optimised pistons, it is possible to compare them in terms of embodied energy and CO_2 emissions. Analysing the graphics seen in Figure 81 (a) and Figure 81 (b), it becomes clear that the base piston exhibits higher energy usage and CO_2 emissions during the material, transport, and especially the use stage, compared to the optimised piston. The increased energy consumption and CO_2 emissions during the material stage are explained by the greater quantity of material necessary to produce the heavier component, as well as by the fact that powder production is only accounted for the manufacturing stage. This justifies why the material stage for the optimised piston is considerably lower. This additional weight also affects the transport phase, as transporting the heavier base piston over the same distance results in higher fuel consumption and consequently increased embodied energy and greenhouse gas emissions. The significantly higher levels of energy and CO_2 associated with the base piston during the usage stage can be explained by the fact that, over the 10-year lifetime of the car, it leads to higher fuel consumption and higher greenhouse gas emissions compared to the optimised piston, which is considerably lighter and therefore results in lower environmental impacts during the usage stage. However, producing these optimised pistons requires more energy, since the process uses a laser, resulting in higher embodied energy, and also relies on inert gases, which increase the greenhouse gas emissions. Furthermore, as already mentioned, powder production was also included in this stage, providing another reason why the manufacturing stage presents such a significant difference in terms of embodied energy and CO_2 emissions between the optimised and base piston.

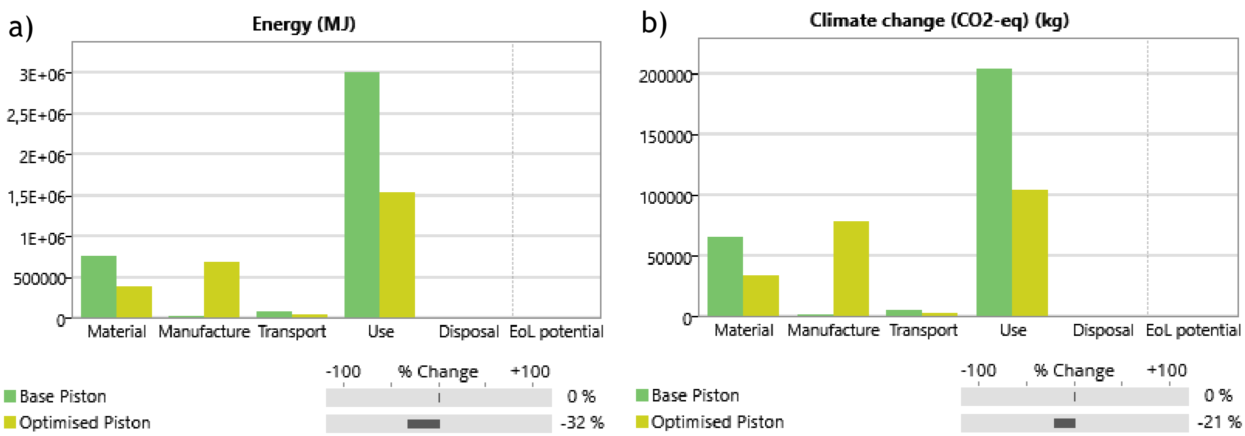

Figure 81: Graphs comparing the base and optimised pistons: (a) Embodied energy; (b) CO_2 emissions.

Directly comparing the values between the base and optimised pistons in terms of embodied energy, it is evident that most energy usage in the base piston is nearly half of what is required to produce the optimised piston, except in the manufacturing stage. In this stage, the energy demand for the optimised pistons drastically increases, rising from 1.96×10^4 MJ to 6.84×10^5 MJ as seen in Table 2. This table also shows that the initial pistons present a total embodied energy of 3.87×10^6 MJ, whereas the optimised versions significantly reduce the total embodied energy to 2.65×10^6 MJ, representing a 32% decrease.

Table 2: Energy usage at each stage and total embodied energy for the base and optimised pistons.

	Energy from Base Pistons (MJ)	Energy from Base Pistons (%)	Energy from Optimised Pistons (MJ)	Energy from Optimised Pistons (%)
Material	7.68×10^5	19.8	3.91×10^5	14.8
Manufacture	1.96×10^4	0.5	6.84×10^5	25.9
Transport	7.72×10^4	2.0	3.93×10^4	1.5
Use	3.01×10^6	77.6	1.53×10^6	57.8
Disposal	1.77×10^3	0.0	9.00×10^2	0.0
Total	3.87×10^6	100	2.65×10^6	100

Focusing now on CO_2 emissions, as in the case of the energy usage, the optimised pistons produce less CO_2-equivalent emissions than the base pistons in all stages, except during manufacturing, where emissions largely increase from 1.47×10^3 kg to 7.89×10^4 kg, as shown in Table 3. The total of CO_2 equivalent emissions for the base pistons is considerably higher than for the optimised versions, amounting to 2.77×10^5 kg and 2.19×10^5 kg, respectively. This represents a 21% reduction.

Table 3: CO_2-equivalent emissions at each stage and total emissions for the base and optimised pistons.

	CO_2-eq emissions from Base Pistons (kg)	CO_2-eq emissions from Base Pistons (%)	CO_2-eq emissions from Optimised Pistons (kg)	CO_2-eq emissions from Optimised Pistons (%)
Material	6.61×10^4	23.8	3.36×10^4	15.3
Manufacture	1.47×10^3	0.5	7.89×10^4	36.0
Transport	5.16×10^3	1.9	2.62×10^3	1.2
Use	2.04×10^5	73.7	1.04×10^5	47.4
Disposal	1.24×10^2	0.0	6.30×10^1	0.0
Total	2.77×10^5	100	2.19×10^5	100

In summary, the optimised piston shows a considerable reduction in environmental impacts, both in terms of embodied energy and CO_2-equivalent emissions, when compared to the base pistons.

4.3.2 Environmental Impact comparison between the Base and Optimised Connecting Rod

The base connecting rods, as previously seen, weigh 0.586 kg each and were assumed to have been produced through forging. As was previously done for the base pistons, the total weight of all components was calculated in order to determine which lorry was most suitable for transporting the connecting rods from Germany to Portugal. For this, Equation 4 was used, where the component weight is 0.586 kg and the number of components is 10000 units, resulting in a total weight of 5860 kg. Therefore, a 3.5 - 7.5t Euro 6 lorry was selected.

In the case of the optimised connecting rods, their weight is 0.40 kg. These components were produced through LPBF, using the same parameters as defined for the optimised piston, with a value of 152 MJ/kg, which also includes the powder and component production. For the CO_2 equivalent emissions, Equation 5 was applied to calculate the CO_2 equivalent emissions in kilograms per component produced, resulting in a value of 2.99 kg CO_2/unit. Considering that the optimised connecting rod weighs 0.40 kg, it was determined that 2.5 units are required to obtain 1 kg of component. Equation 6 was then used to determine the CO_2 equivalent emissions for material extraction, resulting in a total of 7.48 kg CO_2/kg. Finally, the CO_2-equivalent emissions from extraction were subtracted from the 25 kg CO_2-equivalent/kg, obtaining 17.52 kg CO_2-equivalent/kg from powder production and components manufacturing. The 3.5 - 7.5t Euro 6 lorry was also used for transporting the optimised components to ensure a valid comparison in the transport stage.

After defining all the parameters and characteristics for the base and optimised connecting rods, an environmental study focusing on the embodied energy and CO_2-equivalent emissions was conducted. Figure 82 (a) and Figure 82 (b) display graphs comparing each stage in terms of energy usage and CO_2-equivalent emissions, respectively. Overall, the optimised connecting rods demonstrate slightly lower energy usage. However, in terms of CO_2-equivalent emissions, they present a higher overall quantity. As with the optimised piston, both graphs display lower energy consumption and CO_2 equivalent emissions in the material stage for the optimised connecting rod, since less material needs to be extracted and powder production is not included in this stage, but rather in the manufacturing stage. Although energy consumption is relatively high during the manufacturing stage due to the use of lasers, this energy is offset over the component's lifetime. Unfortunately, the same cannot be said for CO_2 emissions, which, despite being lower in all other stages, do not compensate for the quantity of emissions released during the manufacturing stage.

The weight reduction also leads to decreased fuel consumption during transport and over the lifetime of the components, making the sports cars more efficient and reducing their environmental impact in terms of energy usage and CO_2-equivalent emissions.

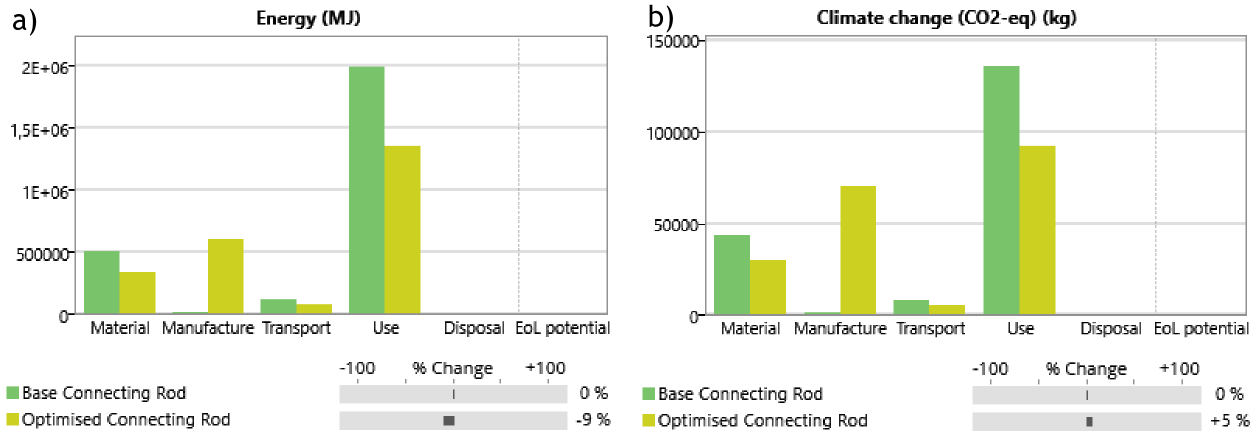

Figure 82: Graphs comparing the base and optimised connecting rods: (a) Embodied energy; (b) CO_2-equivalent emissions.

Focusing now on the direct comparison of the energy usage in each stage between the base and optimised connecting rods, it is possible to confirm from Table 4 that there is a slight reduction in the energy consumption for the optimised connecting rods compared to the base ones. As previously shown in Figure 82 (a), the most significant difference occurs in the manufacturing stage, where the energy usage for the optimised components increases by a factor of 10. However, despite this significant increase in the manufacturing stage, the considerable reductions in the other stages lead to an overall decrease in embodied energy of 9%, declining from an initial value of 2.64×10^6 MJ to 2.40×10^6 MJ.

Table 4: Energy usage at each stage and total embodied energy for the base and optimised connecting rods.

	Energy from Base Connecting Rods (MJ)	Energy from Base Connecting Rods (%)	Energy from Optimised Connecting Rods (MJ)	Energy from Optimised Connecting Rods (%)
Material	5.09×10^5	19.3	3.47×10^5	15.1
Manufacture	1.30×10^4	0.5	6.08×10^5	35.4
Transport	1.22×10^5	4.6	8.33×10^4	2.8
Use	1.99×10^6	75.5	1.36×10^6	46.7
Disposal	1.17×10^3	0.0	8.00×10^2	0.0
Total	2.64×10^6	100	2.40×10^6	100

The results for the CO_2-equivalent emissions seen in Table 5 do not overcome the CO_2-equivalent emissions from the manufacturing stage. The optimised connecting rods display lower CO_2-equivalent emissions in all stages except manufacturing, where the difference is even more pronounced. In the manufacturing stage, the CO_2-equivalent emissions increased from 9.75×10^2 kg to 7.01×10^4 kg, rising from only 0.5% of the total emissions in the base connecting rods to 35.4% in the optimised versions. Unfortunately, this large discrepancy in the optimised connecting rods is not compensated for, displaying a total of 1.98×10^5 kg of CO_2-equivalent emissions, which represents a 5% increase compared to the base connecting rods.

Table 5: CO_2-equivalent emissions at each stage and total emissions for the base and optimised connecting rods.

x	CO_2-eq emissions from Base Connecting Rods (kg)	CO_2-eq emissions from Base Connecting Rods (%)	CO_2-eq emissions from Optimised Connecting Rods (kg)	CO_2-eq emissions from Optimised Connecting Rods (%)
Material	4.38×10^4	23.2	2.99×10^4	15.1
Manufacture	9.75×10^2	0.5	7.01×10^4	35.4
Transport	8.19×10^3	4.3	5.59×10^3	2.8
Use	1.35×10^5	71.9	9.25×10^4	46.7
Disposal	8.20×10^1	0.0	5.60×10^1	0.0
Total	1.89×10^5	100	1.98×10^5	100

Since the weight difference is not as significant as that between the base and optimised pistons, the CO_2-equivalent emissions are higher, and the energy usage does not show as significant a reduction as in the optimised pistons. This means that if the optimisation does not result in a substantial weight reduction, the increased environmental impacts from manufacturing may not be overcome.

4.4 Assembling of the Optimised Components

Before assembling, it was necessary to model a pin to connect the piston and the connecting rod. This pin has a diameter of 20 mm and was extruded to a length of 82 mm, allowing the assembly process to begin.

First, the final version of the optimised connecting rod, seen in Figure 80, was opened in an “Assembling” worksheet in Siemens NX. The “Fix” function was then applied to this component to ensure that it maintained its position during the assembly process. Next, the final version of the optimised piston, Figure 51, was also uploaded into the worksheet, where it was centred and aligned with the upper circumference of the connecting rod. Finally, the previously modelled pin was added to the worksheet, and the “Centre” and “Align” functions were used with the piston. This automatically centred and aligned the pin with the connecting rod, resulting in the assembled components shown in Figure 83.

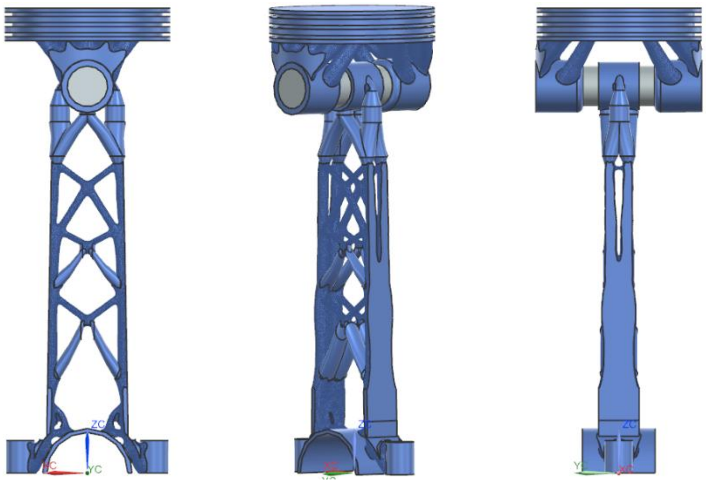

Figure 83: Views of the assembled components.

4.5 Additive Manufacturing Production

4.5.1 Laser Powder Bed Fusion

As mentioned in Chapter 3, the software used to set up the component production in Laser Powder Bed Fusion (LPBF) was Materialise. Initially, it was noted that producing the assembled component as a single piece would result in supports that would be impossible to remove. To avoid this, the optimised piston and connecting rod were exported as separate files. Then, the scale function was applied to both components with a value of 0.25 to fit them within the available base of the LPBF machine, which has a diameter of 30 mm and a maximum producing height of 60 mm.

Focusing on the piston, it was rotated 180 º so that the upper flat surface was in contact with the LPBF base, facilitating the printing process. Afterwards, the only generated supports were those between the LPBF base and the piston's upper flat surface. This approach minimised material usage and allowed for easier removal. Next, the machine's parameters were configured, such as setting a layer thickness of 30.00 µm. Once completed, the file was sent to the LPBF.

Before producing the optimised piston in the LPBF, it was required to ensure the machine was properly cleaned by removing leftover powder, reducing the risk of contamination. After setting everything up, the production process began, taking more than two hours to be completed. After the manufacturing process was completed, the LPBF base was raised, revealing the optimised piston surrounded by unfused powder, as seen in Figure 84.

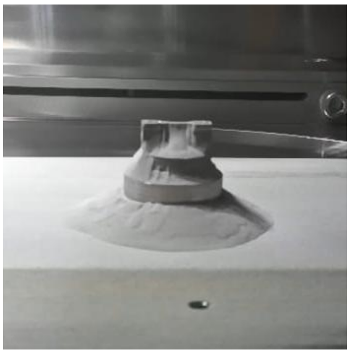

Figure 84: Optimised piston covered with unfused powder in LPBF.

The unused powder was then cautiously removed, cleaning the inside of the machine. Figure 85 displays the geometry obtained after the production of the optimised piston, which is fused to the LPBF base.

Figure 85: Cleaned, optimised piston fused to the LPBF base.

In order to separate the piston from the LPBF base, Electrical Discharge Machining (EDM) was applied. This resulted in only the supports on the flat surface of the piston remaining attached to the base, as shown in Figure 86. These supports were then removed, making the base reusable for future LPBF productions.

Figure 86: Optimised piston separated from the LPBF base.

For the optimised connecting rod, the build orientation was kept in its original position. Line-type supports were chosen for the optimised connecting rod, with only a few between the LPBF base and the component. The machine parameters were configured, and the file was then sent to the LPBF to initiate the production process. Considering that the LPBF machine had already been cleaned, the process was initiated and took more than seven hours to complete. Unfortunately, when the production of the optimised connecting rod was nearly finished, the powder supply ran out, requiring a refill. After this, the production process continued normally until completion. The base was then raised, revealing the optimised connecting rod covered in unused powder, as seen in Figure 87.

Figure 87: Optimised connecting rod covered with unfused powder in LPBF.

Afterwards, the unfused powder between the optimised geometry was removed, along with the remaining powder spread throughout the LPBF machine. Once the machine was properly cleaned, the base was removed, revealing the optimised connecting rod in detail, along with the supports used on its lower part, as seen in Figure 88. The next step, as with the optimised piston, was to separate the base from the optimised component and remove the line-type supports.

Figure 88: Cleaned, optimised connecting rod fused to the LPBF base.

4.5.2 Fused Filament Fabrication

As mentioned in Chapter 3, the Bambu software was used for Fused Filament Fabrication (FFF) printing to produce four components. One was a piston pin scaled to 0.25, manufactured to fit in the already produced optimised metallic piston and connecting rod, and it was set in a vertical position for printing. The other three components manufactured were another piston pin, an optimised piston and connecting rod, this time scaled to 0.50. The production positioning for each component matched that of the 0.25 scale versions, with the piston pin and connecting rod printed in a vertical position and the piston rotated by 180 °. All four components were printed simultaneously using the same production parameters. Supports were generated for the optimised piston and connecting rod, resulting in the tree supports shown in Figure 89. PLA, as previously referred, was used as the printing material, and the FFF production process was then initiated.

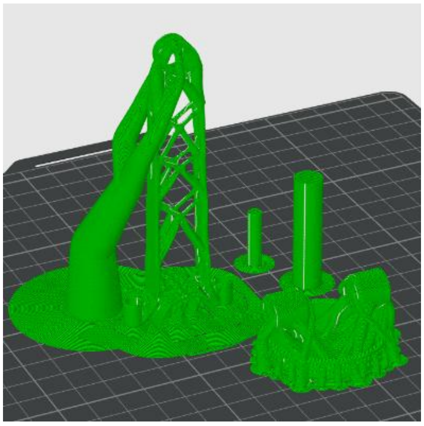

Figure 89: Supports originated for the optimised piston and connecting rod.

Following the conclusion of the manufacturing process for the four components, each one was removed from the base. In the case of the optimised piston and connecting rod, the supports were also manually removed.

4.5.3 Assembling

Starting with the components scaled to 0.25, it was necessary to drill the piston holes to fit the piston pin, as there was some internal material that prevented the pin from being inserted. The same drilling was done on the upper circumference of the connecting rod. After removing this, all the circumferences were slightly widened to facilitate the pin insertion. Once the drilling was completed, all three components were assembled. As shown in Figure 90, the assembled model is reduced in size, and the piston rings are not visible because the used process does not allow for their production. However, this was the only geometric issue observed in the optimised components. Despite the complexity of the geometries, no other geometrical problems were found in either the optimised piston or connecting rod.

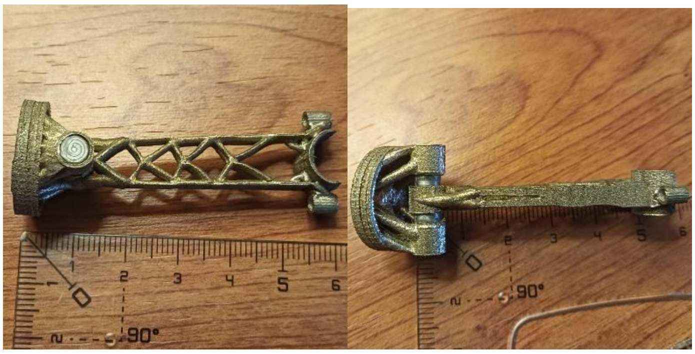

Figure 90: Assembled components scaled to 0.25.

In the case of the PLA components scaled to 0.50, such as the assembly shown in Figure 90, it was also necessary to widen the upper circumferences of the optimised piston and connecting rod. Instead of drilling, which would damage the polymeric structure, sandpaper was rolled and inserted into the interior of the component's upper circumferences to slightly widen them and allow the piston pin to enter more smoothly.

Figure 91 shows the assembled optimised components and the piston pin. The larger scale allows for a more detailed analysis of the geometry compared to the metallic additively manufactured components. However, the area where the piston rings would normally be placed still displays some geometric imperfections due to the presence of supports that could not be removed.

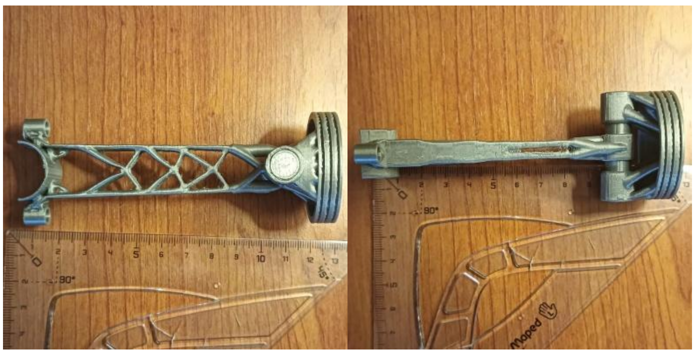

Figure 91: Assembled components scaled to 0.50.

Although both versions present some minor geometric issues, this geometry would not be possible to produce using traditional methods due to its complexity, displaying another advantage of additive manufacturing over conventional processes.

5 CONCLUSIONS

In summary, the piston and connecting rod were topologically optimised. Starting with the piston, its best iteration displays a maximum displacement value of 0.0800 mm when subjected to vertical forces of 40800 N, while weighing only 0.45 kg. Similarly, the superior version of the optimised connecting rod exhibits a maximum displacement of 0.215 mm under the same vertical forces combined with diagonal forces of 23556 N, weighing solely 0.40 kg.

In conclusion, it can be affirmed that both optimisations were a success, as they represent improvements over the base components. In the case of the optimised piston, it displays a significant weight reduction of 49.10% and a 35.48% reduction in maximum displacement. The optimised connecting rod also exhibits reductions of 31.74% in weight and 8.51% in maximum displacement compared to the base component. These reductions in maximum displacement values indicate an increased capacity to withstand applied forces. Weight reduction is also a crucial factor, as it can lead to improved performance and reduced environmental impacts.

Regarding environmental impacts, the study assumes a production of 10000 units of each component, identical transportation methods, and the components are intended to be used for 10 years in a sports car. Focusing on energy usage, the optimised piston and connecting rod both outperform their respective base components, whereas in terms of CO_2-equivalent emissions, only the optimised piston shows a decrease. In other studies, the increased energy consumption or emissions from the manufacturing stage are compensated for, but in the case of the emissions of the connecting rod, this is not the case. Overall, the optimised piston demonstrates a 32% reduction in energy usage and a 21% reduction in CO_2-equivalent emissions, while the optimised connecting rod presents a 9% reduction in energy consumption but a 5% increase in CO_2-equivalent emissions. From this, it is possible to conclude that if optimisation does not result in a significant weight reduction, the increased environmental impacts from manufacturing may not be offset. Furthermore, if an optimised component has a shorter expected lifetime, it may not be environmentally advantageous to use it, even if it is slightly lighter, because of the increased energy consumption and, essentially, CO2-equivalent emissions.

Therefore, it can be concluded that, in addition to the optimised components presenting lower maximum displacement and reduced weight, which, as previously mentioned, positively influence vehicle performance, the weight reduction can also contribute to lowering the environmental impacts of the optimised components.

Concerning the optimised components produced by LPBF, their manufacturing was successful, as the components were obtained without supports except for those separating the optimised component from the LPBF base. Furthermore, the resulting geometries coincided with the modelled designs and allowed for the proper assembling of the components. Regarding the optimised components produced by FFF, the objective was to examine the geometrical characteristics of these components in greater detail.

Overall, this work can be considered a great success, having achieved great results in the areas already mentioned. However, before these components can be introduced into practical applications, further investigation is required. This should begin with analyses of stress concentrations, which must then be minimised. Following this, fatigue simulations in Abaqus should be conducted to assess the number of cycles the optimised components can complete without mechanical compromises. Additionally, prototypes with the real dimensions of the optimised components should be produced and subjected to fatigue tests, with the results compared against those from the Abaqus simulations.

REFERENCES

[1] Nova one Advisor. 04/2025. ‘Internal Combustion Engine Market Size, Share & Trends Analysis Report By Fuel Type (Petroleum, Natural Gas), By End-use (Automotive, Marine, Aircraft), By Region- Global Industry Analysis, Share, Growth, Regional Outlook and Forecasts, 2024-2033’. Accessed: 20/08/2025. Available: https://www.novaoneadvisor.com/report/internal-combustion-engine-market.

[2] Grand View Research. ‘Internal Combustion Engine Market Size, Share & Trends Report Internal Combustion Engine Market Size, Share & Trends Analysis Report By Fuel Type (Petroleum, Natural Gas), By End-use (Automotive, Marine, Aircraft), By Region, And Segment Forecasts, 2023 - 2030’. Accessed: 20/08/2025. Available: https://www.grandviewresearch.com/industry-analysis/internal-combustion-engine-market#.

[3] W. Frazier. 08/04/2014. ‘Metal Additive Manufacturing: A Review’, in *Journal of Materials Engineering and Performance*, vol. 23, pp. 1917–1928.

[4] R. V. Basshuysen and F. Schäfer. 2004. Internal Combustion Engine Handbook Basics, Components, Systems, and Perspectives. Third ed. USA: SAE International, 2004.

[5] F. A. Williams. 2003. ‘Combustion’, in Encyclopedia of Physical Science and Technology. Elsevier, pp. 315–338.

[6] N. Strachan. 2004. ‘Distributed Energy, Overview’, in Encyclopedia of Energy. Elsevier, pp. 823–839.

[7] MechLesson. 01/09/2024. ‘What is Two-Stroke Engine? It Parts, Diagram, & How it Works’. Accessed: 26/02/2025. Available: https://mechlesson.com/two-stroke-engine/.

[8] J. B. Heywood and E. Sher. 1999. ‘OVERVIEW, BACKGROUND, AND HISTORY’, in Two-Stroke Cycle Engine: Its Development, Operation and Design, 1st ed., pp. 3–41. New York: Taylor & Francis.

[9] Yamaha. ‘2stroke / 4stroke’. Accessed: 26/02/2025. Available: https://global.yamaha-motor.com/business/mc/mc-tech/standard-technology/2st4st.html.

[10] MendMotor. ‘What is a Four-Stroke Engine?- Parts, And Working?’. Accessed: 27/02/2025. Available: https://www.mendmotor.com/what-is-four-stroke-engine/

[11] G. Balich and C. Aschenbach. 06/05/2004. ‘The Gasoline 4-Stroke Engine for Automobiles’. University of Notre Dame, Department of Aerospace and Mechanical Engineering.

[12] A. Rajpurohit, K. Patel, J. Naik, M. Bhatt, M. Sondagar, and S. Kushwah. 2021. ‘Design and Analysis of Piston Comparing Different Materials’, in *Recent Advances in Manufacturing Modelling and Optimization*, pp. 689–696. Singapore: Springer.

[13] S. Sabhadiya. 2016. ‘What is a Piston?- Definition, Parts, and Types’. Accessed: 11/03/2025. Available: https://www.theengineeringchoice.com/what-is-piston/.

[14] K. Wannatong, S. Chanchaona, and S. Sanitjai. 01/2008. ‘Simulation algorithm for piston ring dynamics’, in *Simulation Modelling Practice and Theory*, vol. 16, pp. 127–146.

[15] S. Kowalski, B. Cies´likowski, D. Barta, J. Dižo, and A. Dittrich. 03/2023. ‘Analysis

of the Operational Wear of the Combustion Engine Piston Pin’, in *Lubrificants*, vol. 11.
[16] MAHLE GmbH. 2012. ‘Piston function, requirements, and types’, in *Pistons and engine testing*, 1st ed., pp. 1–24. Germany: MAHLE GmbH.
[17] A. Youssef, G. Calderbank, I. Sherrington, E. H. Smith, and H. Rahnejat. 01/2021. ‘A Critical Review of Approaches to the Design of FloatingLiner Apparatus for Instantaneous Piston Assembly Friction Measurement’, in *Lubrificants*, vol. 9 (1), no. 10.
[18] Speedway motors. 2024. ‘Types of Pistons Explained | Dished vs Domed | Forged vs Cast’. Accessed: 13/03/2025. Available: https://www.speedwaymotors.com/the-toolbox/types-of-pistons-explained-dished-vs-domed-forged-vs-cast/137323?srsltid=AfmBOoreWvhIAkYHnzlaFjGY1UfggwqCfmAyllxXQweHSOxhmJVFQACF
[19] M. V. Radchenko, V. G. Radchenko, Yu. O. Shevtsov, and K. S. Krovyakov. 2008. ‘Using electron beam technologies for welding, hardening and surfacing in diesel engineering’, in *Welding International*, vol. 22, pp. 118–121.
[20] K. S. Kumar. 07/2016. ‘DESIGN AND ANALYSIS OF I.C. ENGINEPISTON AND PISTON-RING ON’, in *Journal of Engineering and Science*, vol. 1, pp. 39–51.
[21] MAHLE GmbH. 2012. ‘Piston materials’, in *Pistons and engine testing*, 1st ed., pp. 59–82. Germany: MAHLE GmbH.
[22] DCM. 30/03/2023. ‘What are Cast Pistons – Cast Pistons vs Forged Pistons, What’s the Difference’. Accessed: 17/03/2025. Available: https://www.diecasting-mould.com/news/what-are-cast-pistons-cast-pistons-vs-forged-pistons-whats-the-difference.
[23] S. A. Naik. 08/2014. ‘Design & Shape Optimization of Connecting Rod using FEA: A review’, in *International Journal of Engineering and Technical Research (IJETR)*, vol. 2, pp. 95–100.
[24] J. D. Ramani, S. Shukla, and P. K. Sharma. 03/2014. ‘FE-Analysis of Connecting Rod of I.C.Engine by Using Ansys for Material Optimization’, in *Int. Journal of Engineering Research and Applications*, vol. 4, pp. 216–220.
[25] L. L. Myagkov, K. Mahkamov, N. D. Chainov, and I. Makhkamova. 2014. ‘Advanced and conventional internal combustion engine materials’, in *Alternative Fuels and Advanced Vehicle Technologies for Improved Environmental Performance*, pp. 370–392. Woodhead Publishing Limited.
[26] S. R. E. Hosseini and Z. Li. 2016. ‘Pack Carburizing: Characteristics, Microstructure, and Modeling’, in *Encyclopedia of Iron, Steel, and Their Alloys*, 1st ed.. Boca Raton: Taylor & Francis.
[27] C. H. Schilling. 2001. ‘Colloid Casting’, in *Encyclopedia of Materials: Science and Technology*, 2nd ed., pp. 1314–1319. New York: Elsevier.
[28] H. Yamagata. 2005. ‘The piston ring’, in *The Science and Technology of Materials in Automotive Engines*, 1st ed., pp. 87–109. Woodhead Publishing Limited.
[29] J. Wu, O. Sigmund, and J. P. Groen. 03/2021. ‘Topology optimization of multi-scale structures a review’, in *Structural and Multidisciplinary Optimization*, vol. 63, pp. 1455–1480.

[30] Siemens. 05/2023. ‘Topology Optimization: Part One | NX Tips and Tricks’. Accessed: 20/08/2025. Available: https://blogs.sw.siemens.com/nx-design/topology-optimization-nx-tips-tricks/#section_0.
[31] H. Chung, J. T. Hwang, J. S. Gray, and H. Alicia Kim. 2018. ‘Implementation of topology optimization using openMDAO’, presented at the AIAA Science and Technology Forum and Exposition, Kissimmee, Florida.
[32] Z. Houta, T. Huguet, N. Lebbe, and F. Messine. 2024. ‘Solid Isotropic Material with Penalization-Based Topology Optimization of Three-Dimensional Magnetic Circuits with Mechanical Constraints’, in *Mathematics*, vol. 12 (8), no. 1147.
[33] G. Capasso, J. Morlier, M. Charlotte, and S. Coniglio. 2020. ‘Stress-based topology optimization of compliant mechanisms using nonlinear mechanics’, in *Mechanics & Industry*, vol. 21 (3), no. 304.
[34] S. Kant Ratnakar, S. Sanfui, and D. Sharma. 2021. ‘SIMP-Based Structural Topology Optimization Using Unstructured Mesh on GPU’, in *Advances in Interdisciplinary Engineering*, 1st ed.. Singapore: Springer.
[35] V. Kandemir, O. Dogan, and U. Yaman. 2018. ‘Topology optimization of 2.5D parts using the SIMP method with a variable thickness approach’, in *Procedia Manufacturing*, vol. 17, pp. 29–36.
[36] J. M. Costa, E. W. Sequeiros, D. Figueiredo, A. R. Reis, and M. F. Vieira. 2025. ‘Optimizing Metal AM Potential through DfAM: Design, Performance, and Industrial Impact’, in *Additive Manufacturing - Present and Sustainable Future, Materials and Applications*. Intechopen.
[37] M. Dinar and D. W. Rosen. 02/2017. ‘A Design for Additive Manufacturing Ontology’, in *JOURNAL OF COMPUTING AND INFORMATION SCIENCE IN ENGINEERING*, vol. 17 (2), no. 021013.
[38] C. Klahn, B. Leutenecker, and M. Meboldt. 2014. ‘Design for Additive Manufacturing – Supporting the Substitution of Components in Series Products’, in *Procedia CIRP*, vol. 21, pp. 138–143.
[39] I. Gibson, D. Rosen, B. Stucker, and M. Khorasani. 11/2020. ‘Design for Additive Manufacturing’, in *Additive Manufacturing Technologies*, 3rd ed., pp. 555–607. Switzerland: Springer Cham.
[40] S. Giulio Barbieri, M. Giacopini, V. Mangeruga, and S. Mantovani. 2017. ‘A design strategy based on topology optimization techniques for an additive manufactured high performance engine piston’, in *Procedia Manufacturing*, vol. 11, pp. 641–649.
[41] G. Shanmugasundar, M. Dharanidharan, D. Vishwa, and A. P. Sanjeev Kumar. 2021. ‘Design, analysis and topology optimization of connecting rod’, in *Materials Today: Proceedings*, vol. 46 Part 9, pp. 3430–3438.
[42] S. Kokare, J. P. Oliveira, and R. Godina. 06/2023. ‘Life cycle assessment of additive manufacturing processes: A review’, in *Journal of Manufacturing Systems*, vol. 68, pp. 536-559.
[43] ISO. 2006. *ISO 14044:2006 Environmental management — Life cycle assessment — Requirements and guidelines*. Available: https://www.iso.org/standard/38498.html.
[44] R. Rahmani, B. Bashiri, S. I. Lopes, A. Hussain, H. S. Maurya, and R. Vilu. 2025.

‘Sustainable Additive Manufacturing An Overview on Life Cycle Impacts and Cost Efficiency of Laser Powder Bed Fusion’, in *Journal of Manufacturing and Materials Processing*, vol. 9 (1), no. 18.
[45] T. Peng, K. Kellens, R. Tang, C. Chen, and G. Chen. 05/2018. ‘Sustainability of additive manufacturing: An overview on its energy demand and environmental impact’, in *Additive Manufacturing*, vol. 21, pp. 694–704.
[46] S. Ford and M. Despeisse. 11/2016. ‘Additive manufacturing and sustainability: an exploratory study of the advantages and challenges’, in *Journal of Cleaner Production*, vol. 137, pp. 1573–1587.
[47] F. Calignano and V. Mercurio. 06/2023. ‘An overview of the impact of additive manufacturing on supply chain, reshoring, and sustainability’, in *Cleaner Logistics and Supply Chain*, vol. 7, no. 100103.
[48] M. Akbari. 10/2023. ‘Data-driven review of additive manufacturing on supply chains: Regionalization, key research themes and future directions’, in *Computers & Industrial Engineering*, vol. 184, no. 109600.
[49] R. D. A. Wahab and A. H. Azman. 2019. ‘Additive Manufacturing for Repair and Restoration in Remanufacturing An Overview from Object Design and Systems Perspectives’, in *Processes*, vol. 7 (11), no. 802.
[50] S. Yang, W. Min, J. Ghibaudo, and Y. F. Zhao. 09/2019. ‘Understanding the sustainability potential of part consolidation design supported by additive manufacturing’, in *Journal of Cleaner Production*, vol. 232, pp. 722–738.
[51] J. K. Yin Lee, H. Gholami, A. A. Salameh, and A. Gunasekaran. 2025. ‘Strategies to overcome barriers to LCA adoption in additive manufacturing’, in *Technology in Society*, vol. 83, no. 102980.
[52] S. Ehmsen, J. Conrads, M. Klar, and J. C. Aurich. 2025. ‘Environmental impact of powder production for additive manufacturing: Carbon footprint and cumulative energy demand of gas atomization’, in *Journal of Manufacturing Systems*, vol. 82, pp. 13–25.
[53] N. Afshar-Mohajer, C.-Y. Wu, T. Ladun, D. A. Rajon, and Y. Huang. 11/2025. ‘Characterization of particulate matters and total VOC emissions from a binder jetting 3D printer’, in *Building and Environment*, vol. 93 Part 2, pp. 293–301.
[54] J. Iñaki Arrizubieta, O. Ukar, M. Ostolaza, and A. Mugica. 2020. ‘Study of the Environmental Implications of Using Metal Powder in Additive Manufacturing and Its Handling’, in *Metals*, vol. 10 (2), no. 261.
[55] G. Omar Barrionuevo, J. Andrade-Garzón, L. Llatance-Guevara, and F. E. Alarcón. 2025. ‘Life Cycle Assessment of Tensile Specimens of Stainless Steel Obtained by Additive Manufacturing versus Conventional Manufacturing’, in *Advanced Materials & Sustainable Manufacturing*, vol. 2 (1), no. 10004.
[56] S. Jung, L. Burak Kara, Z. Nie, T. W. Simpson, and K. S. Whitefoot. 04/2023. ‘Is Additive Manufacturing an Environmentally and EconomicallyPreferred Alternative for Mass Production’, in *Environmental Science & Technology*, vol. 57 (16), pp. 6373–6386.
[57] I. Gibson, D. Rosen, B. Stucker, and M. Khorasani. 2021. ‘Introduction and Basic Principles’, in *Additive Manufacturing Technologies*, 3rd ed., pp. 1-22. Switzerland:

Springer Cham.
[58] ISO. 2021. *ISO/ASTM 52900:2021 Additive manufacturing — General principles — Terminology*. Available: https://www.iso.org/standard/69669.html
[59] Prototal UK. 07/10/2022. 'The History Of Additive Manufacturing: From The 1980s to Today'. Accessed: 29/04/2025. Available: https://prototaluk.com/blog/history-of-additive-manufacturing/.
[60] M. Scorianz, L. Guariento, and D. A. Campanacci. 2022. 'The 3D Printing Production Procedure', in *3D Printing in Bone Surgery*, 1st ed., pp. 25–37. Switzerland: Springer Cham.
[61] XYZdims. 6/12/2020. '3D Printer History (1980-2024)'. Accessed: 29/04/2025. Available: https://xyzdims.com/tag/hideo-kodama/.
[62] Markforged. 2022. 'Additive Manufacturing History: From the 1980's to Now'. Accessed: 29/04/2025. Available: https://markforged.com/resources/blog/additive-manufacturing-history.
[63] Z. Miller, B. Stidham, T. Fairbanks, and C. Maldonado. 11/03/2023. 'The Use of Stereolithography (SLA) Additive Manufacturing in Space Based Instrumentation', presented at the IEEE Conference on Aerospace, Big Sky, Montana, USA.
[64] C. Hull. 12/2025. 'The Birth of 3D Printing', in *Research-Technology Management*, vol. 58, pp. 25–30.
[65] E. Pei, I. Rumana Kabir, and B. Leutenecker-Twelsiek. 10/2023. 'History of AM', in *Springer Handbook of Additive Manufacturing*, 1st ed., pp. 3–29. Switzerland: Springer Cham.
[66] J. Beaman. 2021. 'Historical background', in *Fundamentals of Laser Powder Bed Fusion of Metals*, 1st ed., pp. 1–14. Elsevier.
[67] S. Cem Altiparmak, V. Yardley, Z. Shi, and J. Lin. 11/2022. 'Extrusion-based additive manufacturing technologies: State of the art and future perspectives', in *Journal of Manufacturing Processes*, vol. 83, pp. 607–636.
[68] H. Almeida and J. Vasco. 09/2019. 'Expectations of Additive Manufacturing for the Decade 2020–2030', in *Progress in Digital and Physical Manufacturing,* 1st ed., pp. 10–19 Switzerland: Springer Cham.
[69] M. Attaran. 10/2017. 'The rise of 3-D printing: The advantages of additive manufacturing over traditional manufacturing', in *Business Horizons*, vol. 60, pp. 677–688.
[70] B. Durakovic. 12/2018. 'Design for Additive Manufacturing: Benefits, Trends and Challenges', in *Periodicals of Engineering and Natural Sciences*, vol. 6, no. 2, pp. 179–191.
[71] L. Li, X. Zhang, T. Pan, and F. Liou. 11/2021. 'Component repair using additive manufacturing experiments and thermal modeling', in *The International Journal of Advanced Manufacturing Technology*, vol. 119, pp. 719–732.
[72] R. Kennedy. 08/08/2019. 'Outside the Box: How GE Aviation Entered the Brave New World of Additive Manufacturing'. Accessed: 14/04/2025. Available: https://www.geaerospace.com/news/articles/100-year-anniversary-manufacturing-technology/outside-box-how-ge-aviation-entered-brave.

[73] S. Kumar. 06/2023. ‘Advantage and Disadvantage’, in *Additive Manufacturing Advantage*, 1st ed., pp. 1-60. Switzerland: Springer Cham.

[74] A. Bhatia and A. Kumar Sehgal. 2023. ‘Additive manufacturing materials, methods and applications: A review’, in *Materials Today: Proceedings*, vol. 81, Part 2, pp. 1060–1067.

[75] N. Hasan Dipu. 12/2024 ‘An overview of additive manufacturing technology generic processes, fundamental categories, advantages, disadvantages, and applications’.

[76] X. Guo, J. Zhou, W. Zhang, Z. Du, C. Liu, and Y. Liu. 08/2017. ‘Self-supporting structure design in additive manufacturing through explicit topology optimization’, in *Computer Methods in Applied Mechanics and Engineering*, vol. 323, pp. 27–63.

[77] Y. Kok *et al*. 02/2018. ‘Anisotropy and heterogeneity of microstructure and mechanical properties in metal additive manufacturing: A critical review’, in *Materials & Design* vol. 139, pp. 565–586.

[78] N. N. Kumbhar and A. V. Mulay. 08/2016. ‘Post Processing Methods used to Improve Surface Finish of Products which are Manufactured by Additive Manufacturing Technologies A Review’, in *Journal of The Institution of Engineers (India): Series C*, vol. 99, pp. 481–487.

[79] M. Kahvazi Zadeh, M. Yeganeh, M. Tavakoli Shoushtari, H. Ramezanalizadeh, and F. Seidi. 06/2022. ‘Microstructure, corrosion behavior, and biocompatibility of Ti-6Al-4 V alloy fabricated by LPBF and EBM techniques’, in *Materials Today Communications*, vol. 31, no. 103502.

[80] G. Shi, R. Zhang, Y. Cao, and G. Yang. 06/2024. ‘A Review of the Vaporization Behavior of Some Metal Elements in the LPBF Process’, in *Micromachines*, vol. 15, no. 846.

[81] J. Wang, R. Zhu, Y. Liu, and L. Zhang. 10/2023. ‘Understanding melt pool characteristics in laser powder bed fusion: An overview of single- and multi-track melt pools for process optimization’, in *Advanced Powder Materials*, vol. 2 (4), no. 100137.

[82] K. Safaei *et al.*. 10/2021. ‘Additive Manufacturing of NiTi Shape Memory Alloy for Biomedical Applications Review of the LPBF Process Ecosystem’, in *Additive Manufacturing for Medical Applications,* vol. 73, pp. 3771–3786.

[83] E. De Leon, A. Riensche, B. D. Bevans, C. Billings, Z. Siddique, and Y. Liu. 01/2025. ‘A Review of Modeling, Simulation, and Process Qualification of Additively Manufactured Metal Components via the Laser Powder Bed Fusion Method’, in *Journal of Manufacturing and Materials Processing*, vol. 9 (1), no. 22.

[84] G. O. Barrionuevo, M. Walczak, J. Ramos-Grez, and X. Sánchez-Sánchez. 07/2023. ‘Microhardness and wear resistance in materials manufactured by laser powder bed fusion: Machine learning approach for property prediction’, in *CIRP Journal of Manufacturing Science and Technology*, vol. 43, pp. 106–114.

[85] C. Gayer *et al.*. 08/2019. ‘Development of a solvent-free polylactide/calcium carbonate composite for selective laser sintering of bone tissue engineering scaffolds’, in *Materials Science and Engineering: C*, vol. 101, pp. 660–673.

[86] S. Ramadurga Narasimharaju *et al.*. 03/2022. ‘A comprehensive review on laser powder bed fusion of steels: Processing, microstructure, defects and control methods,

mechanical properties, current challenges and future trends', in *Journal of Manufacturing Processes*, vol. 75, pp. 375–414.
[87] C.-P. Jiang, Masrurotin, A. Toto Wibisono, W. Macek, and M. Ramezani. 2025. 'Enhancing Internal Cooling Channel Design in Inconel 718 Turbine Blades via Laser Powder Bed Fusion A Comprehensive Review of Surface Topography Enhancements', in *International Journal of Precision Engineering and Manufacturing*, vol. 26, pp. 487–511.
[88] Y. Zeynep Mandev, E. Mandev, and A. Fatih Yetim. 2025. 'Effects of Laser Powder Bed Fusion Process Parameters on Porosity, Liquid Retention, and Thermal and Surface Properties for 316L, CoCrW and Ti6Al4V Alloys', in *Journal of Materials Engineering and Performance*, vol. 34, pp. 4240–4255.
[89] M. Singh Khandpur, A. Giubilini, L. Iuliano, and P. Minetola. 2024. 'On the Use of Green and Blue Laser Sources for Powder Bed Fusion State of the Art Review for Additive Manufacturing of Copper and Its Alloys', in *Metals*, vol. 14 (12), no. 1464.
[90] S. García-Rodríguez, J. Bedmar, N. Abu-warda, B. Torres, and J. Rams. 08/2024. 'Microstructure and corrosion behavior of 316L stainless steel lattice and bulk parts manufactured by LPBF using fiber and CO2 lasers', in *Materials & Design*, vol. 244, no. 113214.
[91] K. Riener *et al.*. 10/2019. 'Influence of particle size distribution and morphology on the properties of the powder feedstock as well as of AlSi10Mg parts produced by laser powder bed fusion (LPBF)', in *Additive Manufacturing*, vol. 34, no. 101286.
[92] J. Yin *et al.*. 10/2019. 'High-power laser-matter interaction during laser powder bed fusion', in *Additive Manufacturing*, vol. 29, no. 100778.
[93] W. Guo *et al.*. 03/2022. 'Effect of laser scanning speed on the microstructure, phase transformation and mechanical property of NiTi alloys fabricated by LPBF', in *Materials & Design*, vol. 215, no. 110460.
[94] L. Li *et al.*. 01/2024. 'Effect of hatch spacing on the characteristics of LPBF 2195 Al-Li alloy', in *Journal of Alloys and Compounds*, vol. 972, no. 172804.
[95] M. Badrossamay, A. Rezaei, E. Foroozmehr, A. Maleki, and A. Foroozmehr. 10/2021. 'Effects of increasing powder layer thickness on the microstructure, mechanical properties, and failure mechanism of IN718 superalloy fabricated by laser powder bed fusion', in *The International Journal of Advanced Manufacturing Technology*, vol. 118, pp. 1703–1717.
[96] F. AHMADI, J. Song, and R. ZOUGHI. 07/2024. 'Electromagnetic Scattering Properties of Metal Powder Cloud for Laser Powder Bed Fusion (LPBF) Additive Manufacturing (AM)', in *IEEE Open Journal of Antennas and Propagation*, vol. 5 (6), pp. 1639–1648.
[97] L. Guo *et al.*. 12/2023. 'Identifying the keyhole stability and pore formation mechanisms in laser powder bed fusion additive manufacturing', in *Journal of Materials Processing Technology*, vol. 321, no. 118153.
[98] T. Debroy *et al.*. 2018. 'Additive manufacturing of metallic components – Process, structure and properties', in *Progress in Materials Science*, vol. 92, p. 112.224.
[99] L. Guo *et al.*. 01/2023. 'Understanding keyhole induced-porosities in laser powder

bed fusion of aluminum and elimination strategy', in *International Journal of Machine Tools and Manufacture*, vol. 184, no. 103977.

[100] N. Chukwunenye Igwe, I. Akhrif, and M. El Jai. 2025. 'Failure modes analysis and assessment of aluminum-based metallic matrix composites printed with LPBF technology', in *The International Journal of Advanced Manufacturing Technology*, vol. 138, pp. 3621-3647.

[101] D. Wang, L. Liu, G. Deng, C. Deng, Y. Bai, and Y. Yang. 2022. 'Recent progress on additive manufacturing of multi-material structures with laser powder bed fusion', in *Virtual and Physical Prototyping*, vol. 17, pp. 329–365.

[102] D. W. Gibbons, P. Govender, and A. F. van der Merwe. 2024. 'Metal powder feedstock evaluation and management for powder bed fusion a review of literature, standards, and practical guidelines', in *Progress in Additive Manufacturing*, vol. 9, pp. 805–833.

[103] M. Dadkhah, M. Hossein Mosallanejad, L. Iuliano, and A. Saboori. 2021. 'A Comprehensive Overview on the Latest Progress in the Additive Manufacturing of Metal Matrix Composites Potential, Challenges, and Feasible Solutions', in *Acta Metallurgica Sinica (English Letters)*, vol. 34, pp. 1173–1200.

[104] E. L. Li, L. Wang, A. B. Yu, and Z. Y. Zhou. 03/2021. 'A three-phase model for simulation of heat transfer and melt pool behaviour in laser powder bed fusion process', in *Powder Technology*, vol. 381, pp. 298–312.

[105] A. Asgarian, Z. Tang, M. Bussmannb Department of Mec, and K. Chattopadhyay. 2020. 'Water atomisation of metal powders Effect of water spray configuration', in *Powder Metallurgy*, vol. 63, pp. 288–299.

[106] K. Kassym and A. Perveen. 2020. 'Atomization processes of metal powders for 3D printing', in *Materials Today: Proceedings*, vol. 26, Part 2, pp. 1727–1733.

[107] L. E. T. Mathias *et al.*. 2024. 'Metal powder as feedstock for laser-based additive manufacturing From production to powder modification', in *Journal of Materials Research*, vol. 39, pp. 19–47.

[108] N. Zapparoli. 2021. 'Comparison between the surface roughness and mechanical properties of AISI 316L samples produced via Laser Powder Bed Fusion process using gas atomized and water atomized powders'. Master's dissertation, Politecnico di Torino.

[109] F. Persson, C. Neil Hulme, and P. G. Jönsson. 01/2022. 'Particle morphology of water atomised iron-carbon powders', in *Powder Technology*, vol. 397, no. 116993.

[110] M. Hossein Sehhat, A. T. Sutton, C.-H. Hung, J. W. Newkirk, and M. C. Leu. 2022. 'Investigation of Mechanical Properties of Parts Fabricated with Gas- and Water-Atomized 304L Stainless Steel Powder in the Laser Powder Bed Fusion Process', in *JOM*, vol. 74, pp. 1088–1095.

[111] M. Xu, H. Guo, Y. Wang, Y. Hou, Z. Dong, and L. Zhang. 2023. 'Mechanical properties and microstructural characteristics of 316L stainless steel fabricated by laser powder bed fusion and binder jetting', in *Journal of Materials Research and Technology*, vol. 24, pp. 4427–4439.

[112] D. D'Andrea. 2023. 'Additive Manufacturing of AISI 316L Stainless Steel A Review',

in *Metals*, vol. 13 (8), no. 1370.

[113] Md. Shamsujjoha, S. R. Agnew, J. M. Fitz-Gerald, W. R. Moore, and T. A. Newman. 2018. 'High Strength and Ductility of Additively Manufactured 316L Stainless Steel Explained', in *Metallurgical and Materials Transactions A*, vol. 49, pp. 3011–3027.

[114] C. Alex Sumanariu, C. Gheorghe Amza, F. Baciu, M. Ion Vasile, and A. Ionut Nicoara. 2024. 'Comparative Analysis of Mechanical Properties: Conventional vs. Additive Manufacturing for Stainless Steel 316L', in *Materials*, vol. 17 (19), no. 4808.

[115] Truer. 'Best Stainless Steel 316L Powder For 3D Printing'. Accessed: 22/08/2025. Available: https://am-printing.com/stainless-steel-316l-powder-20231124.

[116] S. Can Erman, A. Aydin, K. Groom, and K. Mumtaz. 01/2025. 'Diode area melting of SS316L using low power 450 nm lasers', in *The International Journal of Advanced Manufacturing Technology*, vol. 136, pp. 4471–4490.

[117] A. H. Ettefagh, S. Guo, and J. Raush. 01/2021. 'Corrosion performance of additively manufactured stainless steel parts: A review', in *Additive Manufacturing*, vol. 37, no. 101689.

[118] G. Kumar Meenashisundaram, Z. Xe, M. L. Sharon Nai, S. Lu, J. Sheuan Ten, and J. Wei. 2020. 'Binder Jetting Additive Manufacturing of High Porosity 316L Stainless Steel Metal Foams', in *Materials*, vol. 13 (17), no. 3744.

[119] R. He *et al.*. 11/2022. 'In silico evaluation of additively manufactured 316L stainless steel stent in a patient-specific coronary artery', in *Medical Engineering & Physics*, vol. 109, no. 103909.

[120] M. S. Alam *et al.*. 2025. 'Additively manufactured 316L stainless steel as a potential alternative implant material', in *Journal of Materials Research and Technology* vol. 34, pp. 2358–2373.

[121] J. I. Ahuir-Torres *et al.*. 2024. 'A Study of the Corrosion Resistance of 316L Stainless Steel Manufactured by Powder Bed Laser Additive Manufacturing', in *Applied Science*, vol. 14 (17), no. 7471.

[122] P. I. Pradeep *et al.*. 2020. 'Characterization and Qualification of LPBF Additively Manufactured AISI-316L Stainless Steel Brackets for Aerospace Application', in *Transactions of the Indian National Academy of Engineering*, vol. 5, pp. 603–6016.

[123] H3D. 19/04/2024. 'Superior Performance of Stainless Steel 316L in Automotive Engine Components Manufacturing'. Accessed: 19/04/2025. Available: https://en.hb3dp.com/news/221.html.

[124] Y. Zhang, A. A. Amin Daman, P. He, X. Li, P. Borghesani, and Z. Peng. 01/2025. 'Wear study of additively manufactured 316L stainless steel gears', in *Wear*, vol. 571, no. 205796.

[125] J. Gonzalez-Gutierrez, S. Cano, S. Schuschnigg, C. Kukla, J. Sapkota, and C. Holzer. 05/2018. 'Additive Manufacturing of Metallic and Ceramic Components by the Material Extrusion of Highly-Filled Polymers: A Review and Future Perspectives', in *Materiais*, vol. 11 (5), no. 840.

[126] D. Fico, D. Rizzo, R. Casciaro, and C. Esposito Corcione. 01/2022. 'A Review of Polymer-Based Materials for Fused Filament Fabrication (FFF): Focus on Sustainability and Recycled Materials', in *Polymers*, vol. 14 (3), no. 465.

[127] B. Brenken, E. Barocio, A. Favaloro, V. Kunc, and R. Byron Pipes. 05/2018. ‘Fused filament fabrication of fiber-reinforced polymers: A review’, in *Additive Manufacturing*, vol. 21, pp. 1–16.

[128] A. Rodríguez-Panes, J. Claver, and A. María Camacho. 08/2018. ‘The Influence of Manufacturing Parameters on the Mechanical Behaviour of PLA and ABS Pieces Manufactured by FDM: A Comparative Analysis’, in *Materials*, vol. 11 (8), no. 1333.

[129] A. Dey, I. Eagle, and N. Yodo. 06/2021. ‘A Review on Filament Materials for Fused Filament Fabrication’, in *Journal of Manufacturing and Materials Processing*, vol. 5 (3), no. 69.

[130] Bergsen Metals. 12/01/2021. ‘316 vs 316L Stainless Steel: What’s the Difference?’. Accessed: 29/05/2025. Available: https://bergsen.com/316-vs-316l-stainless-steel/.

[131] Nickel Institute. 2020. ‘Design guidelines for the Selection and use of stainless steels’, in *A DESIGNERS’ HANDBOOK SERIES*. AISI.

[132] J. E. Bringas. 2004. ‘Introduction to Comparing World Steel Standards’, in *Handbook of Comparative World Steel Standards*, 3rd ed., pp. 1–19. USA: ASTM.

[133] G. O. Barrionuevo, J. Andrade-Garzón, L. Llatance-Guevara, and F. E. Alarcón. 2025. ‘Life Cycle Assessment of Tensile Specimens of Stainless Steel Obtained by Additive Manufacturing versus Conventional Manufacturing’, in *Advanced Materials & Sustainable Manufacturing*, vol. 2 (1), no. 10004.

[134] C. van Sice and J. Faludi. 06/2021. ‘Comparing environmental impacts of metal additive manufacturing to conventional manufacturing’, in *Proceedings of the Design Society*, vol. 67, pp. 671–680.

[135] A. Baroutaji, A. Arjunan, J. Robinson, A. Vance, and A. Arafat. 06/2025. ‘Critical Review on the Sustainability of Metal Additive Manufacturing: Environmental and Economic Perspectives’, in *Renewable and Sustainable Energy Technology*.